

A Fast and Robust Poisson–Boltzmann Solver Based on Adaptive Cartesian Grids

Alexander H. Boschitsch^{*,†} and Marcia O. Fenley^{*,‡}

[†]Continuum Dynamics, Inc., 34 Lexington Ave., Ewing, New Jersey 08618, United States

[‡]Department of Physics and Institute of Molecular Biophysics, Florida State University, Tallahassee, Florida 32306-3408, United States

 Supporting Information

ABSTRACT: An adaptive Cartesian grid (ACG) concept is presented for the fast and robust numerical solution of the 3D Poisson–Boltzmann equation (PBE) governing the electrostatic interactions of large-scale biomolecules and highly charged biomolecular assemblies such as ribosomes and viruses. The ACG offers numerous advantages over competing grid topologies such as regular 3D lattices and unstructured grids. For very large biological molecules and their assemblies, the total number of grid points is several orders of magnitude less than that required in a conventional lattice grid used in the current PBE solvers, thus allowing the end user to obtain accurate and stable nonlinear PBE solutions on a desktop computer. Compared to tetrahedral-based unstructured grids, ACG offers a simpler hierarchical grid structure, which is naturally suited to multigrid, relieves indirect addressing requirements, and uses fewer neighboring nodes in the finite difference stencils. Construction of the ACG and determination of the dielectric/ionic maps are straightforward and fast and require minimal user intervention. Charge singularities are eliminated by reformulating the problem to produce the reaction field potential in the molecular interior and the total electrostatic potential in the exterior ionic solvent region. This approach minimizes grid dependency and alleviates the need for fine grid spacing near atomic charge sites. The technical portion of this paper contains three parts. First, the ACG and its construction for general biomolecular geometries are described. Next, a discrete approximation to the PBE upon this mesh is derived. Finally, the overall solution procedure and multigrid implementation are summarized. Results obtained with the ACG-based PBE solver are presented for (i) a low dielectric spherical cavity, containing interior point charges, embedded in a high dielectric ionic solvent—analytical solutions are available for this case, thus allowing rigorous assessment of the solution accuracy; (ii) a pair of low dielectric charged spheres embedded in an ionic solvent to compute electrostatic interaction free energies as a function of the distance between sphere centers; (iii) surface potentials of proteins, nucleic acids, and their larger-scale assemblies such as ribosomes; and (iv) electrostatic solvation free energies and their salt sensitivities—obtained with both linear and nonlinear Poisson–Boltzmann equations—for a large set of proteins. These latter results along with timings can serve as benchmarks for comparing the performance of different PBE solvers.

INTRODUCTION

The efficient and accurate implicit solvent-based electrostatic modeling of large complex and highly charged biomolecules in an aqueous electrolyte solution at finite ionic strengths remains an important and difficult challenge in computational molecular biophysics. Considerable success in modeling the long-range and nonspecific electrostatic interactions of biomolecules in ionic solution has been achieved on the basis of the Poisson–Boltzmann equation (PBE), which provides the electrostatic potential and other important derived quantities (e.g., electrostatic solvation free energies, electrostatic binding free energies, forces, and pK shifts) under varying ionic conditions.¹ Nevertheless, two challenges persist in the numerical calculation of such systems. First, for large molecules, the mesh topologies used to date—regular lattices and unstructured tetrahedral grids—are subject to various inefficiencies and/or mesh generation challenges that can be improved upon by considering an alternate mesh structure as well as selecting a representation of the solution that reduces the mesh resolution demands. In the current development, the PBE is solved upon a hierarchical mesh structure variously referred to as an adaptive Cartesian grid

(ACG) or octree or simply a Cartesian mesh. The ACG terminology is adopted here to distinguish it from regular lattices, which are also commonly called Cartesian grids. The second challenge is achieving reliable and rapid solution convergence for highly charged biomolecular systems. The current article describes a methodology that addresses both challenges, resulting in a robust nonlinear PBE analysis capable of properly modeling salt-mediated and nonspecific electrostatic effects in nucleic acids and their associations with charged ligands such as cationic drugs, peptides, and larger proteins.

One goal of the ACG-based PBE solver is to facilitate computation of electrostatic properties for large-scale biomolecular systems at the atomic level of detail using readily accessible computational resources. For example, a recent experimental study suggests that the electrostatic interactions in the ribosomal exit tunnel can modulate the elongation rates of nascent peptides.² For such large-scale ribosomal systems, most Poisson–Boltzmann studies have necessarily been based on coarse-grained molecular

Received: December 4, 2010

Published: April 15, 2011

models due to memory constraints and convergence issues.³ The PBE solver described here provides the variable mesh spacing necessary to efficiently accommodate such nanoscale biomolecular assemblies. Moreover, it contains robust iterative procedures that reliably converge the electrostatic solution at comparable rates for both the linear and nonlinear PBE of highly charged complex biomolecular systems such as ribosomes. This property is used to obtain a high resolution (0.3 Å) surface potential map of the highly charged large 50S ribosomal subunit. To the best of our knowledge, nonlinear PBE calculations for such a highly charged and large biomolecular system have not been previously performed on a serial platform—at least at such a fine grid resolution. Moreover, with the computational tools developed here, nonlinear PB calculations can be conducted in nearly the same amount of computer time as linear ones, as borne out in the Supporting Information, which provides such timings for a collection of proteins.

Solution Methods for the PBE. Numerical solutions to the PBE can be obtained using either finite difference (FD) techniques, which here include finite element (e.g., unstructured tetrahedral meshes) and finite volume-based discretizations, or boundary element methods (BEM). Each approach has inherent advantages, as reviewed in refs 1 and 4. Briefly, when solving the linear PBE using the BEM, (i) only a surface mesh is required, since the solution is expressed entirely in terms of surface distributions; (ii) far-field boundary conditions are automatically satisfied; (iii) the constraints upon the electrostatic potential and its normal gradient at the molecular surface are explicitly imposed; (iv) the potential fields associated with point charges are expressed analytically, thereby circumventing problems relating to representing singular solutions upon grids; and (v) the interactions between distant elements are evaluated using the exact expressions, thus conferring high accuracy. With the introduction of fast multipole methods, computational costs have been reduced from $O(N^2)$ to $O(N \log N)$ (N being the number of boundary elements), thus allowing much larger problems to be addressed. The first PBE solvers utilizing fast multipole-accelerated BEM were limited to zero salt conditions.^{5–7} The extension to finite salt concentrations was first achieved by Boschitsch and co-workers^{4,8} and subsequently by Lu and co-workers using a different form of the fast multipole expansion.^{9,10}

A major limitation of BEM-based approaches is the forfeiture of a pure surface-based solution representation and the attendant increase in computational effort when solving the nonlinear form of the PBE. Our experience¹¹ has consistently shown that even for very simple cases, computation times can easily increase by $O(10)$ – (100) when using the BEM for the linear part and nonlinear terms expressed as source distributions, where the latter appear as volume integrals over the entire computational domain. Hybrid schemes offer one venue for retaining the advantages of a BEM while allowing the nonlinear PBE to be addressed.¹¹

In the FD method, the differential form of the equations is solved on a volume mesh that fills the region of interest. The discrete equations can be derived according to variational principles which underlie the finite element (FE) method or by classical finite difference schemes based on the Taylor series expansions about a given mesh point. The FE method provides a general and systematic approach for developing the discrete model upon a variety of meshes including unstructured (tetrahedral) and curvilinear grids. In some instances however, the FD method offers a more efficient approximation. For example, when adopting a

regular lattice mesh, the FD approximation to the Laplacian operator at a mesh point both is second-order accurate and involves only six neighboring mesh points, whereas a FE model is only first-order accurate (at least in the most common implementations^{12,13} using linear order tetrahedral elements) and involves all 26 neighboring mesh points, thus increasing computational requirements.

The mesh structure employed in a FD method directly influences the performance and the quality of the results obtained. Historically, FD-based PBE modeling has employed two basic grid structures:

Regular 3D Lattice. This is the grid arrangement adopted in the popular PBE solvers such as APBS,¹⁴ UHBD,¹⁵ PBEQ,¹⁶ MEAD,¹⁷ ZAP,¹⁸ DelPhi,¹⁹ and PBSA-Amber^{20–22} and consists of a uniformly spaced rectangular grid superimposed over the biomolecule of interest. While no attempt is made to align the mesh with the molecular surface, good estimates of the electrostatic potential solution are nevertheless obtained because this solution is continuous across the surface. Regular lattices allow one to readily develop a simple and efficient discretization of the differential operators and to implement effective multigrid procedures. However, the lack of a variable or adaptive grid spacing capability leads to a restrictive tradeoff between accuracy and storage constraints as larger biomolecules are considered. Furthermore, to minimize errors generated at the outer boundary of the grid (such errors introduce biases in computed electrostatic potential and energies), the grid must be extended sufficiently far from the molecule so that the potential at the outer boundaries is negligible. Nonlinear PBE calculations of highly charged biomolecular systems are especially challenging in this regard since consistent outer-boundary treatments for the nonlinear PBE have only recently become available.²³ To reduce calculation effort and maintain good accuracy, the focusing²⁴ procedure is invoked where the solution obtained on a global mesh with large mesh spacing is interpolated onto a collection of finer, localized grids. This approach improves local accuracy but entails multiple PBE calculations for a given molecular configuration.

Unstructured Grids. To address the shortcomings of regular lattice grids, efforts have been directed at the use of unstructured tetrahedral grids for biomolecules (e.g., ref 25). Such grids can achieve good resolution over a wide range of length scales and also offer the opportunity for solution-dependent mesh adaptation. Unstructured grids have been used in the finite element solution of the PBE to produce accurate predictions of biomolecular electrostatic properties.^{12,13,25} A useful feature of unstructured grids is the ability to conform to the molecular surface so that no edges or elements intersect the surface. This allows for inherently more accurate estimates of surface properties, particularly the electrostatic field, which is essential for reliable prediction of electrostatic PBE forces. On the other hand, unstructured meshes are subject to several limitations: (i) The generation of good quality meshes is complex and time-consuming, especially for grids that conform to the molecular boundary; however active research in this area is expected to reduce the associated computation times.²⁶ (ii) Neighboring nodes must be explicitly identified, thus increasing storage costs (each node has approximately 14 neighbors, compared to six on a regular lattice grid). (iii) Mesh adaptation procedures are complex and expensive due to the large number of refinement possibilities in 3D. (iv) Multigrid implementation is challenging because defining coarser level meshes and linear-order accurate (the minimum order needed for second-order PDEs) interpolation procedures

between multigrid levels is nontrivial. (v) The discrete approximation to the PBE equation generally has first-order errors (errors are $O(h)$ where h is the local mesh spacing) compared to the approximation on a regular lattice, which is second-order accurate (errors are $O(h^2)$), so that slower convergence with mesh spacing is obtained.

Herein, an alternate grid structure is proposed that combines the adaptation and variable resolution features of unstructured grids with the simple cube geometry and multigrid capabilities enjoyed by regular lattice methods. This mesh, referred to here as an adaptive Cartesian grid, derives from the hierarchical decomposition of the computational domain known as an octree,²⁷ which is obtained by recursive and selective subdivision of a cube into smaller nested cubes (see for example Figure 2). It is noted that an article utilizing the ACG concept to solve the nonlinear PBE has recently appeared²⁸ to model supercapacitor behavior of porous electrodes. Their approach embodies several of the same methodology details described below, including the derivation of the finite difference formulas. Their applications do not appear to call for a decomposition of the solution to eliminate singular behavior at charge sites, and applications were limited to comparatively simple geometries. ACGs have been widely used in fluid mechanics applications to model flows about complex geometries.^{29,30} Often, the most time-consuming and challenging task in such applications is constructing a good quality mesh (for a complex geometry, this can require several man-months), and ACGs were developed in response to the need for a fast and fully automated grid-generation capability.^{31–33} Like unstructured grids, the ACG allows the analysis to “zoom” into regions where the solution is varying rapidly—e.g., near the molecular surface. Elsewhere, where variations are more gradual, fewer, larger cells may be used for optimal computational efficiency. Outer boundaries can be placed far from the molecular boundary to minimize the influence of boundary errors without incurring appreciable computational cost. Compared to unstructured grids, the ACG generation and adaptation procedures are both simpler and less expensive computationally (for example, a mesh containing a million nodes is easily generated in under a minute using standard nonoptimized code on a readily accessible PC hardware). Finally, ACG facilitates implementation of multigrid schemes since the underlying octree data structure already prescribes a complete hierarchy of coarser level meshes and linearly accurate interpolation between levels is readily achieved.

In addition to using an ACG, the PBE solution methodology presented here adopts a decomposition of the electrostatic potential field similar to that in ref 34 to eliminate the singularities at fixed atomic charge sites. In the exterior regions, the usual total electrostatic potential is computed. Inside the molecule, one develops the reaction field potential which contains no singularities and so is accurately resolved on a mesh. The interior and exterior solutions are connected by calculating the Coulombic potential for nodes near the molecular boundary using fast multipole acceleration methods.⁸ By eliminating the singularities, this decomposition (i) increases overall accuracy and reduces sensitivity to grid translations/rotations, (ii) alleviates mesh spacing requirements (no refinement near charge sites is required), and (iii) allows one to directly and accurately compute total electrostatic free energies (the grid-dependent self-energies³⁵ are completely absent) and forces. An interesting consequence of i is that the regions where the computed solution varies most rapidly are at the molecular surface rather than at atomic charge sites. This implies that the finest mesh spacing is

warranted at the surface, and coarser elements can be employed away from the surface.

The sections below describe the generation of the ACG mesh; the discrete approximation of the Poisson–Boltzmann equation on this grid, including the decomposition of the solution into the full and reaction field potentials and the imposition of outer boundary conditions; the solution procedure using Gauss–Seidel iteration and multigrid; and postprocessing operations. Results are obtained using the ACG-based PBE solver for classical idealized problems involving one and two low dielectric spheres, containing interior charges to affirm the overall accuracy of the method, high resolution calculations of the electrostatic potential and other important derived electrostatic properties for medium-sized biomolecules, and demonstration calculations for a selected large-scale and highly charged ribosome. In the Supporting Information, ACG-PB predictions of electrostatic solvation free energies are provided for a variety of proteins with varying size, shape, and charge density along with timing information for both linear and nonlinear PB solutions.

■ METHODOLOGY

Generation of the ACG. Generation of the ACG grid for a given molecular structure presumes availability of the atomic coordinates (ρ_k), radii (σ_k), and partial charges (Q_k). The atomic coordinates can be obtained from structural biology databases such as the RCSB Protein Data Bank (PDB files) or Nucleic Acid Database (NDB files). The atomic radii can be assigned using one of many available atomic radii sets (e.g., Bondi³⁶). Assigning atomic charges is more involved, especially when proper protonation state assignment is required, but typically either a formal charge set is adopted or partial atomic charges derived from molecular mechanics force fields, such as AMBER³⁷ or CHARMM,³⁸ are used. In addition to this structural description, a molecular surface definition must also be specified. Common surface definitions available in the ACG generation software include the van der Waals (vdW) surface, which is the exposed surface of the collection of overlapping spheres, and the solvent-excluded (SE) surface (also commonly referred to as the molecular or Connolly surface) obtained by rolling a probe sphere of radius, r_{probe} (usually, $r_{\text{probe}} = 1.4 \text{ \AA}$ for water), over the van der Waals surface and identifying the points which can be reached by the probe (exterior points) and which ones cannot (interior). Other surface definitions, such as various Gaussian function-based descriptions (e.g., ref 39), can also be used and are available in the ACG software. Developing the ACG and assigning the dielectric map to the resulting mesh nodes requires the ability to determine whether a given point lies within the molecular surface. For the vdW surface, this determination is straightforward using an inside-sphere test. For the SE surface, the test is somewhat more involved—here, the procedures described by Chan and Purisima⁴⁰ are employed.

The ACG generation process begins by placing an initial cube over the entire molecule. This initial cube is sized to be several times larger than the maximum dimension of the molecule so that the boundary condition at the outer boundary can be accurately imposed (see below). The cube is then uniformly subdivided a fixed number of times, L , to produce a uniform lattice starting mesh containing $(2^L + 1)^3$ nodes (or 8^L cube-shaped cells).

Recursive adaptation of this initial mesh then proceeds by identifying which individual mesh cells intersect the molecular

surface. Each intersected cell is tested to determine whether one of the following refinement criteria is satisfied:

- (i) the user-specified finest mesh spacing, Δ_{\min} , is reached or
- (ii) the intersected cell lies more than a prescribed distance from the nearest atomic charge site.

Each intersected cell that does not meet either of these criteria is uniformly subdivided into eight smaller cells. The resulting ACG is then again subjected to these mesh intersection and refinement tests and the grid generation process continued. The refinement process naturally terminates since eventually all intersected cells meet the refinement criteria i or ii.

To prevent excessive cell size variation that can be detrimental to solutions accuracy, the ACG is smoothed by requiring that no terminal cell (a cell that has not been refined into smaller ones) be larger than twice any of its neighbors. This requirement also facilitates development of the finite difference procedures and implementation of multigrid. If requested, a Stern or ion exclusion layer of specified thickness, t , is defined by appropriately marking all nodes that are outside the molecule and less than a distance, t , away from the nearest interior node.

When conducting electrostatic interaction or binding energy calculations where the electrostatic energy of, say, a charged ligand–nucleic acid complex is subtracted from the electrostatic energies of the charged ligand and nucleic acid considered in isolation, all three calculations (charged ligand, nucleic acid, and charged ligand–nucleic acid pair) are conducted on the same mesh. This is because the electrostatic interaction or binding energy is often several orders of magnitude smaller than the individual electrostatic energy contributions so that small errors (e.g., due to finite mesh size) in the individual electrostatic energies appear large relative to the electrostatic interaction energy. In such calculations, the ACG is generated with respect to all three geometries as if the molecule actually consisted of the superposition of all three molecular surfaces. The same mesh is then employed for all three energy calculations using the respective dielectric maps.

Finite Differencing on the ACG. The ACG contains “hanging” nodes, which are nodes that neighbor an element but are not a vertex of that element (for example, a node that lies on a midedge or the face of an element). The presence of hanging nodes complicates the application of a variational or finite element framework for deriving the governing equations (specifically, compatibility between different sized elements is not easily enforced). For this reason, a finite difference approach is adopted to obtain a discrete expression of the PBE on the ACG. In developing a FD approximation to the weighted Laplacian, $\nabla \cdot (\epsilon \nabla \Phi)$, it is desirable to simultaneously achieve the following properties: (i) compactness, to ensure robust convergence and numerical stability, the formula should be compact (i.e., only involve immediately neighboring nodes); (ii) consistency, as mesh spacing is reduced, the difference formula should converge to the exact analytical result; (iii) positive weights, the final expression relates the potential at a point, i , to the weighted sum of the neighboring node potentials; ensuring that the associated weights are positive is important for stable convergence and conformance with maximum principles for elliptic PDEs.⁴¹ An additional consideration for continuum electrostatic modeling is that the dielectric “constant” changes discontinuously at the molecular surface (MS). This makes it difficult to develop formally consistent FD rules. However, the errors committed

in applying the FD formulas near the MS can be viewed as perturbations of the surface geometry. Also, the success of FD applied upon regular lattices indicates that good PBE predictions can be obtained with simple interpolation of the dielectric/ionic map (e.g., as currently done in any of the lattice code such as APBS). Here, we will adopt such interpolation schemes and confirm their effectiveness by subsequent numerical studies. Current work is being directed at addressing accurate interpolation at the surface.

The FD method begins by distinguishing between various types of nodes. Denoting the collection of terminal octree cells, i_b , that touch a node, i , by $\{N_i\} = \{i_b: i_b \text{ incident to node, } i\}$ (this implies that node i lies on the surface of i_b), then three types of mesh nodes can be distinguished.

Type 0 Node i is a *vertex* of all terminal cells, $i_b \in \{N_i\}$, which implies that it is *not* a hanging node. Type 0 nodes are further distinguished into two subtypes:

Type 0A All $i_b \in \{N_i\}$ are of equal size.

Type 0B The members $i_b \in \{N_i\}$ differ in size.

Type 1 The node lies on the *midedge* of at least one terminal cell, $i_b \in \{N_i\}$.

Type 2 The node lies on the *face* center of exactly one terminal cell, $i_b \in \{N_i\}$.

Examples of these nodes are shown in Figure 1. Note that type 1 and 2 nodes are necessarily adjacent to cells of differing size. Also, in all cases, the members of $\{N_i\}$ differ by no more than a factor of 2 in size. Finally, each node can only be of one type (e.g., it cannot simultaneously lie on a midedge and a face center). This is a result of the size constraint between neighboring cells. Under these constraints, the finite difference expressions for the differential operator, $\partial/(\partial x)(\epsilon(\partial\Phi)/(\partial x))$, are now developed for each of the node types.

The finite differencing expression for type 0A nodes is the same as that used on a regular lattice. Along the x direction, the contribution to $\nabla \cdot (\epsilon \nabla \phi)$ is

$$\frac{\partial}{\partial x} \left(\epsilon \frac{\partial \Phi}{\partial x} \right)_i = \bar{\epsilon}_{i,i+1} \frac{(\Phi_{i+1} - \Phi_i)}{\Delta x^2} - \bar{\epsilon}_{i,i-1} \frac{(\Phi_i - \Phi_{i-1})}{\Delta x^2} + O(\Delta x^2) \quad (1)$$

where \mathbf{R}_i is the position of node i , $\phi_i = \phi(\mathbf{R}_i)$, $\mathbf{R}_{i\pm 1} = \mathbf{R}_i \pm \mathbf{i}(\Delta x)$, \mathbf{i} is the unit vector along x , and Δx is the size of the surrounding cells. The second-order error estimate, $O(\Delta x^2)$, formally only applies when the dielectric constant is not changing, which is the case away from the molecular surface. The dielectric constant, $\bar{\epsilon}_{i,i+1}$, is evaluated at the connecting edge midpoint.

Referring to Figure 1, the unique consistent finite difference formula at a type 0B node involving the triplet of collinear nodes, $\{0, 1, 2\}$, is

$$\frac{\partial}{\partial x} \left(\epsilon \frac{\partial \Phi}{\partial x} \right)_1 = \bar{\epsilon}_{1,2} \frac{\Phi_2 - \Phi_1}{3\Delta x^2} - 2\bar{\epsilon}_{0,1} \frac{\Phi_1 - \Phi_0}{3\Delta x^2} + O(\Delta x) \quad (2)$$

where Φ_i is the value of Φ at the indicated vertex. Note that the formula is only first-order accurate.

The FD formulas for type 1 and type 2 nodes are developed by identifying the neighboring nodes, developing Taylor series expansions for these nodes, and then considering how to combine these series so that only the desired second-order derivatives remain. For type 1 nodes such as node M in Figure 1, this process

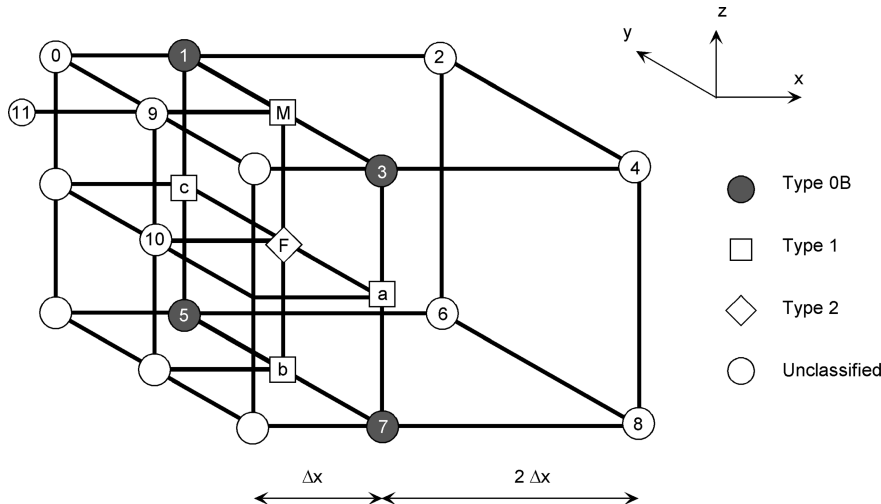


Figure 1. ACG nodes lying on the interface between two different sized cells.

leads to the first order formula:

$$\frac{\partial}{\partial x} \left(\varepsilon \frac{\partial \Phi}{\partial x} \right)_M = \varepsilon(R_{c1}) \frac{1}{3\Delta x^2} \left(\frac{\Phi_2 + \Phi_4}{2} - \frac{\Phi_1 + \Phi_3}{2} \right) - 2\bar{\varepsilon}_{M,9} \left(\frac{\varphi_M - \varphi_9}{3\Delta x^2} \right) + O(\Delta x) \quad (3)$$

where the center of the face formed from nodes 1–2–3–4,

$$R_{c1} = \frac{R_1 + R_2 + R_3 + R_4}{4} \quad (4)$$

For a type 2 node such as node F in Figure 1, one obtains the first order accurate formula:

$$\frac{\partial}{\partial x} \left(\varepsilon \frac{\partial \Phi}{\partial x} \right)_F = \varepsilon(R_{c2}) \frac{1}{3\Delta x^2} (\Delta^+ \Phi) - 2\bar{\varepsilon}_{F,10} \left(\frac{\varphi_F - \varphi_{10}}{3\Delta x^2} \right) + O(\Delta x) \quad (5)$$

where the cell center,

$$R_{c2} = \frac{1}{8} \sum_{k=1}^8 R_k \quad (6)$$

and the central difference approximation to $\partial\Phi/\partial x$ at R_{c2} is

$$\Delta^+ \Phi = \frac{1}{4} (\Phi_2 + \Phi_4 + \Phi_6 + \Phi_8) - \frac{1}{2} (\Phi_M + \Phi_a + \Phi_b + \Phi_c - 2\Phi_F) \quad (7)$$

This form is preferred over other options since it promotes positive weights in the final assembled Laplacian approximation, eq 8.

Summary of the FD Formulas. The FD formulas are first-order accurate (errors are of $O(\Delta x)$) for other than type 0A nodes. It is possible to extend them to higher order by including additional nearby points, but this invites other problems such as nonpositive weights and numerical instability associated with the stronger influence from the more distant neighbors. The finite element method applied using linear elements is also first-order accurate (this is easily demonstrated in 1D when computing $\partial^2 \Phi / \partial x^2$ upon an unevenly spaced grid), whereas the regular

lattice methods are second-order accurate. The ACG-based FD method offers intermediate accuracy since, depending upon the degree of smoothing, the grid is populated mostly with type 0A nodes. Hence, the discretization is second-order accurate over most of the mesh and thus approaches the order of accuracy of a regular lattice.

The FD approximations to the second-order derivatives in the x direction extend naturally to the y and z derivatives which, when assembled, yield the discrete approximation to $\nabla \cdot (\varepsilon \nabla \Phi)$. At a node, i , this approximation can be cast in the form of a weighted sum:

$$(\nabla \cdot \varepsilon \nabla \Phi)_i = \sum_{\text{neighbors}, j} \omega_{ij} (\Phi_j - \Phi_i) \quad (8)$$

where ω_{ij} are the weights. For regions where the dielectric is constant, $\omega_{ij} > 0$. Across the surface where dielectric changes however, some weights for type 1 and type 2 nodes at the molecular surface may become negative, but no convergence issues have occurred in our PBE calculations to date. It is easy to show that this discrete approximation of $\nabla \cdot (\varepsilon \nabla \Phi)$ upon the ACG is compact and consistent, satisfies a discrete maximum principle (all weights, ω_{ij} are positive⁴²), and reverts to the classical finite difference expressions when implemented upon a regular lattice.

Application to the Poisson–Boltzmann Equation. The PBE is expressed over three distinct regions: (i) the molecular interior or solute region, Ω_1 , which contains the atomic point charges, has a low dielectric constant, ε_1 , and is enclosed by the molecular surface defined previously; (ii) the exterior or ionic solvent region, Ω_2 , which has a high dielectric constant, ε_2 , and contains the dissolved ions; and (iii) a charge-free Stern layer (or ion exclusion region where no mobile ions are present), Ω_3 , of specified thickness about the molecular surface with dielectric constant $\varepsilon_3 = \varepsilon_2$. The Stern layer can be used to account for the ion size, and its thickness corresponds roughly to the hydrated radius of the ion. In all PB calculations below, the Stern layer thickness is set to zero.

The reduced (or dimensionless) electrostatic potential of any arbitrary 3D complex-shaped biopolyelectrolyte, Φ , at location \mathbf{R} in the computational domain, is governed by

$$\nabla \cdot [\varepsilon(\mathbf{R}) \nabla \Phi(\mathbf{R})] + \frac{4\pi e}{k_B T} \rho(\mathbf{R}) = 0 \quad (9)$$

where the volume charge density in the different regions is given by

$$\rho(\mathbf{R}) = \rho^f(\mathbf{R}) = \sum_k Q_k \delta(\mathbf{R} - \rho_k), \mathbf{R} \in \Omega_1 \quad (10a)$$

$$\rho(\mathbf{R}) = \rho^m(\mathbf{R}) = -2eI_{1:1} \sinh(\Phi), \mathbf{R} \in \Omega_2 \quad (10b)$$

$$\rho(\mathbf{R}) = 0, \mathbf{R} \in \Omega_3 \quad (10c)$$

Note that the expression for $\rho^m(\mathbf{R})$ in eq 10b pertains to a 1:1 electrolyte solvent (e.g., NaCl), which is assumed here for ease of presentation. The extension to more general salt environments is straightforward, and the ACG-based PBE solver currently accommodates mixtures of 1:1 and 2:1 salts^{11,43} and asymmetric salts.

Introducing the Debye–Hückel screening parameter, κ , as

$$\kappa^2 = \frac{8\pi e^2 I_{1:1}}{\varepsilon_2 k_B T} \quad (11)$$

allows one to rewrite the PBE in the exterior domain, Ω_2 , as

$$\nabla \cdot (\varepsilon \nabla \Phi) = \varepsilon_2 \kappa^2 \sinh(\Phi) \equiv f(\Phi) \quad (12)$$

The linearized form of eq 12, valid for small electrostatic potentials, $\Phi \ll 1$, is obtained by setting $f(\Phi) \approx f_L(\Phi) = \varepsilon_2 \kappa^2 \Phi$.

In the ACG-based FD implementation, a discrete approximation of eq 9 is solved at every mesh node. The discretization of the dielectric-weighted Laplacian, $\nabla \cdot (\varepsilon \nabla \Phi)$, is given by eq 8. For nodes outside the molecule (in Ω_2 and Ω_3), evaluation of the charge density in eq 9 according to eq 10b or 10c is straightforward. However, evaluation of the charge density within the molecular interior presents numerical difficulties because the potential becomes singular at the fixed solute charge sites (i.e., atomic centers), ρ_k . To eliminate this singular behavior, an alternate representation of the interior potential field is adopted.

Representation of the Interior Electrostatic Potential. The interior total electrostatic potential can be expressed as the sum $\Phi = \Phi^{rf} + \Phi^c$, where Φ^{rf} is the reaction field potential satisfying

$$\nabla \cdot [\varepsilon(\mathbf{R}) \nabla \Phi^{rf}(\mathbf{R})] = 0 \quad (\underline{\mathbf{R}} \in \Omega_1) \quad (13)$$

and Φ^c is the singular Coulombic potential given by

$$\Phi^c(\mathbf{R}) = \frac{1}{4\pi} \sum_{\text{charges}, k} \frac{q_k}{|\mathbf{R} - \rho_k|} \quad (14)$$

Here, the reduced charge centered at position ρ_k is $q_k = (4\pi e / \varepsilon_1 k_B T) Q_k$. The reaction field potential contains no singularities and therefore can be accurately resolved on the ACG. Thus, at all interior points, the analysis solves for Φ^{rf} governed by eq 13 rather than Φ . This approach closely resembles the one implemented by Zhou et al.³⁵ upon a regular lattice. In the exterior region, $\Omega_2 \cup \Omega_3$, the full electrostatic potential, Φ , is retained, and eq 9 is solved.

To connect these two representations, Φ^{rf} and Φ , at the dielectric interface, first distinguish between the following four possible arrangements for a grid point, i , and its neighbors, j :

- Point i , and all of its neighbors, j , lie inside the molecular interior, Ω_1 .
- Point i and all of its neighbors, j , lie inside the molecular exterior, $\Omega_2 \cup \Omega_3$.
- Point i lies in the exterior region, $\Omega_2 \cup \Omega_3$, but at least one of its neighbors lies inside the molecule in Ω_1 .

- Point i lies inside Ω_1 , but at least one of its neighbors lies outside the molecule in $\Omega_2 \cup \Omega_3$.

Cases a and b pose no difficulty since the discrete approximation eq 8 can be directly applied without modification. In case c, one solves eq 9 and thus seeks to evaluate $\nabla \cdot (\varepsilon \nabla \Phi)$. Here, the total electrostatic potential is available at node i and all neighbors lying in the exterior domain. However, for those neighbors located inside the interior region, Ω_1 , one has only the reaction field potential. Hence, the Coulombic potential, evaluated according to 14, must be added to these interior grid points before evaluating the weighted Laplacian. Thus, eq 8 is modified to

$$(\nabla \cdot \varepsilon \nabla \Phi)_i = \sum_{\substack{\text{neighbors,} \\ j \in \Omega_2 \cup \Omega_3}} \omega_{ij} (\Phi_j - \Phi_i) + \sum_{\substack{\text{neighbors,} \\ j \in \Omega_1}} \omega_{ij} (\Phi_j^{rf} + \Phi_j^c - \Phi_i) \quad (15)$$

Case d is treated similarly. One can solve eq 13 and subtract Φ^c from all exterior neighbors, j . This option requires evaluating the Coulombic potential at exterior grid points. Alternatively, if both i and its neighbors, j , are sufficiently distant from the nearest charge, then one can instead solve the equation for the full potential, $\nabla \cdot (\varepsilon \nabla \Phi) = 0$. Then, as for case c, the Coulombic potential must be added to each of the interior nodes (including node i) before evaluating the weighted Laplacian.

All cases can be expressed in terms of the generalized potential,

$$\Phi^g(\underline{\mathbf{R}}) = \begin{cases} \Phi^{rf}(\mathbf{R}), & \mathbf{R} \in \Omega_1 \\ \Phi(\mathbf{R}), & \mathbf{R} \in \Omega_2 \cup \Omega_3 \end{cases} \quad (16)$$

which is the discontinuous quantity actually represented upon the ACG mesh. The evaluation of the Laplacian can then be expressed as a weighted summation over all neighbors (without distinction as to whether they lie inside or outside the molecule):

$$(\nabla \cdot \varepsilon \nabla \Phi)_i = \sum_{\text{neighbors, } j} \omega_{ij} (\Phi_j^g - \Phi_i^g) + \sigma_i \quad (17)$$

where σ_i represents the source terms originating from the Coulombic potentials at neighboring *interior* points such as those appearing in 15. Note that the source term is only nonzero for points having one neighbor across the molecular surface. Thus the Coulombic potential need only be evaluated at interior points lying adjacent to the molecular surface, thereby minimizing the number of Coulombic potential evaluations. To further expedite the computation, Φ^c is evaluated using the fast multipole acceleration method.^{4,8,44}

After including the ionic source contributions from the PBE in the exterior region, the final discrete form of the PBE can be written:

$$\lambda_i = \sum_{\text{neighbors, } j} \omega_{ij} (\Phi_j^g - \Phi_i^g) + \sigma_i - f(\Phi_i^g) = 0 \quad (18)$$

where $f_i = f(\Phi_i^g) = 0$ at interior points since one is solving for the reaction field potential there.

Outer Boundary Conditions. The governing equations are closed by specifying the potential at the outer boundary. One option is to set $\Phi = 0$ at the outer boundary and place the outer boundary sufficiently far away to minimize the effects of outer boundary errors—this can be accomplished more readily with the variable mesh spacing features of the ACG. Another option is to evaluate the outer boundary potential using the Debye–Hückel

approximation:

$$\Phi^b \cong \frac{1}{4\pi(\varepsilon_2/\varepsilon_1)} \sum_{\text{charges}, k} \frac{q_k}{|\mathbf{R} - \rho_k|} \exp\{-\kappa|\mathbf{R} - \rho_k|\} \quad (19)$$

which is useful when solving the linear PBE. Solutions to the nonlinear PBE, however, generally decay more quickly away from the surface (where, $|\Phi| > 1$) than their linear counterparts. Thus, when considering the nonlinear PBE, eq 19 tends to overestimate the boundary potentials, which introduces a bias into the computed solution.

The approach²³ adopted here is to approximate the electrostatic potential outside the computational domain by the approximate monopole formula, $\Phi^b = Be^{-\kappa(r-h)}/r$ where the constant, B , is determined from electroneutrality conditions and $2h$ is the side length of the overall grid. This approach is equally valid for both the linear and nonlinear forms of the PBE and requires only that the magnitude of the potential at the outer boundaries $|\Phi| \ll 1$. An explicit expression for B is given elsewhere.²³

Iterative Solution Scheme. The discrete system, eq 18, comprises a sparse algebraic set of coupled equations to be solved for the potentials, Φ_i^g . For large numbers of nodes, direct inversion of the equation system is not feasible, and an iterative inversion method must be used. The choice of iteration method has direct bearing upon the robustness and rate of solution convergence. Here, a standard Gauss–Seidel iteration method and multigrid are combined to achieve the good convergence. Gauss–Seidel iteration usually results in an initially rapid, but then slowed convergence rate. This slackening in convergence is due to the persistence of long wavelength errors. Like most simple iteration schemes, Gauss–Seidel updating effectively eliminates short wavelength errors that fluctuate most rapidly between grid points but is less efficient at removing long wavelength components. To promote faster convergence at moderate computational expense (storage and CPU), multigrid acceleration is employed in the ACG-based PBE solver.

Multigrid methods exploit the error smoothing properties of the Gauss–Seidel iteration process. After several Gauss–Seidel iterations, the short wavelength errors are mostly eliminated, and only long wavelength errors remain. These errors can therefore be accurately resolved upon a coarser grid. Moreover, because the mesh spacing is larger, the errors fluctuate more rapidly between grid points on the coarser mesh. Therefore, Gauss–Seidel applied on the coarser level is more effective at eliminating those errors. This basic insight motivates the multigrid concept, which attempts to eliminate errors over all wavelengths by projecting the solution onto a hierarchy of increasingly coarser meshes. Descriptions of the multigrid method are available elsewhere⁴⁵ (including applications to the PBE^{46,47}). Therefore, only a brief description of the overall method is presented here, with emphasis reserved for those implementation details that are specific to the use of an ACG.

The multigrid algorithm begins by defining a sequence of nested meshes, $\{M' : l = 0, \text{nlev}\}$ where M^0 is the finest level mesh. Next, interpolation procedures for transferring solutions and errors between successive levels are defined. In multigrid terminology, these are referred to as “restriction” (transferring a solution from the finer grid, M'^{-1} , to the coarser level mesh, M'), and “prolongation” (transferring from M' to M'^{-1}) operators. Here bilinear interpolation is employed for the prolongation step and its adjoint operator (full weighting⁴⁵) used for restriction.

In a two-level multigrid implementation, the solution process begins by conducting a series of single-level Gauss–Seidel iterations on the finest level, M^0 . The errors (or residuals), λ_i , from eq 18 are then evaluated and restricted to the next coarser level, $l = 1$, using full weighted averaging. A discrete approximation to the PBE is then developed on this coarser level. However, the Coulombic source terms, σ_i , on this coarser level are set to zero and replaced everywhere by the restricted errors which now “drive” the coarser level solution. Gauss–Seidel iteration is then conducted on this coarser level to obtain a correction potential on this level, $\{\Phi^1\}$. The final step is to linearly interpolate the corrections to the finer level, $l = 0$, and add them to the existing solution, $\{\Phi^0\} = \{\Phi^g\}$. The extension to multiple levels is straightforward and explained elsewhere.^{45–47}

Post-Processing. The total electrostatic free energy expression is taken from eq 8 of ref 48. After integration by parts of the last term and substituting using the governing equation, eq 9, one obtains the total electrostatic free energy, G^{el} , in $k_B T$ units:¹¹

$$G^{\text{el}} = G_f + G_m - \Delta\Pi \quad (20)$$

where

$$G_f = C \int_{\Omega_1} \frac{4\pi e}{k_B T \varepsilon_1} \rho_f \Phi \, dV = C \sum_{\text{charges}, k} q_k \Phi(\underline{\rho}_k) \quad (21a)$$

$$G_m = C \tilde{\varepsilon} \kappa^2 \int_{\Omega_2} \Phi \sinh(\Phi) \, dV \quad (21b)$$

$$\Delta\Pi = C \tilde{\varepsilon} \kappa^2 \int_{\Omega_2} (2\cosh\Phi - 2) \, dV \quad (21c)$$

and the conversion factor to express the energies in $k_B T$ units is

$$C = \frac{(k_B T)^2 \varepsilon_1}{8\pi e^2} \quad (22)$$

Here, G_f is the energy due to fixed charges, and G_m and $\Delta\Pi$ are the electrostatic stress and excess osmotic pressure terms, respectively. The excess osmotic pressure contribution has special significance when assessing salt dependencies of the electrostatic free energies, since one can show^{49,50}

$$\frac{dG^{\text{el}}}{d\kappa} = -\frac{2}{\kappa} \Delta\Pi \quad (23)$$

It is also useful to define the reaction field energy,

$$G_{rf} = \int_{\Omega_1} \frac{4\pi e}{k_B T \varepsilon_1} \rho_f (\Phi - \Phi^c) \, dV = \sum_{\text{charges}, k} q_k \Phi^g(\rho_k) \quad (24)$$

which is the difference between G_f and the Coulombic energy.

For interior points in Ω_1 (e.g., the charge sites, ρ_k), $\Phi = \Phi^c + \Phi^g$, is obtained by interpolating the reaction field potential from the ACG and adding the Coulombic potential, Φ^c , from eq 14. The electrostatic energy contribution from the interior region, G_f , is computed by summing the product of charge times the electrostatic potential at the fixed charge sites. The volume integrals over the exterior region, Ω_2 , are evaluated by looping over the cubic cells, i_b , of the ACG and approximating the volume integral of any function, $g(\Phi)$, by

$$\int_{V_{ib} \cap \Omega_2} g(\Phi) \, dV \cong \frac{\Delta s^3}{8} \sum_{\text{external vertices}, k} g(\Phi_k) \quad (25)$$

where the sum is taken over the exterior forming nodes, k , of cell i_b , and Φ_k is the potential at forming node k . In addition, a correction term is added to the volume integrals to account for the contribution outside the computational domain. This correction term is based on the same monopole approximation used for the outer boundary treatment and is developed fully in ref 23.

■ RESULTS

The results presented here serve two main objectives. The first is to assess error by comparing ACG PBE predictions against analytical solutions or results obtained by alternate highly accurate means.¹¹ In these studies, simple model geometries involving one or two low dielectric spherical cavities, containing charges, embedded in a high dielectric ionic solvent medium are considered. The second goal is to demonstrate the effectiveness of the ACG-based PBE solver as a practical tool for modeling high resolution medium- and large-scale biomolecules ranging from proteins to more highly charged nucleic acids and its large and complex biomolecular assemblies for which numerous X-ray crystal structures are now available. This second goal is accomplished by computing the electrostatic potential maps. Calculations were performed on a Dell Precision M2300 laptop (3 GHz with 4 GB of installed memory) or a dual-processor Intel Xeon Linux workstation (3 GHz with 1 GB of memory).

In addition to the results below, the Supporting Information contains the computed electrostatic (solvation) energies, timings, and scaling with system size for proteins with varying charge densities, shapes, and sizes and modeled both with the linear and the nonlinear PBE. Those results show that for the same system the computation time to solve nonlinear PBE is, on average, 6% more than that for the linear PBE.

Linear PBE Solved for a Low Dielectric Spherical Cavity with a Unit Charge Embedded in a High Dielectric Ionic Solvent. The first model configuration studied solves the linear PBE for a unit radius low dielectric spherical cavity, containing a single interior charge, embedded in 0, 0.1, and 5 M salt solutions. The dielectric constants are set to $\epsilon_1 = 2$ and $\epsilon_2 = 80$, and the temperature is set to $T = 298.15$ K. No ion exclusion or Stern layer is modeled in this or subsequent PBE calculations presented here. Since analytical expressions, developed by Kirkwood,⁵¹ for the solution of the linear Poisson–Boltzmann equation are available for all $\kappa > 0$,^{51,52} this case constitutes a useful benchmark for establishing the overall accuracy of the ACG-PB solver. The computational domain extends over four radii, and the mesh is generated by requiring that any surface-intersected cell whose size is larger than 0.125 times the distance to the nearest charge is subdivided. As the charge is displaced toward the surface, this subdivision criterion produces an increasingly finer mesh about the surface point closest to the unit charge (see Figure 2). The time to complete the calculation for all 15 charge locations was 105 s on the PC laptop machine.

The mesh and contours of constant electrostatic potential for the case where the charge is closest to the surface ($1 - \rho = 3.125 \times 10^{-3}$ Å so that the distance from the surface is 0.3% of the atom radius) are shown in Figure 2. With the variable mesh spacing capability, the full mesh involves only approximately 115 000 mesh points (a comparable resolution calculation on a regular 3D lattice would entail over a trillion points). Note that the finest resolution provided by the ACG PB solver is at the surface nearest the charge, not at the charge itself. This is where the exterior full electrostatic potential and the interior reaction

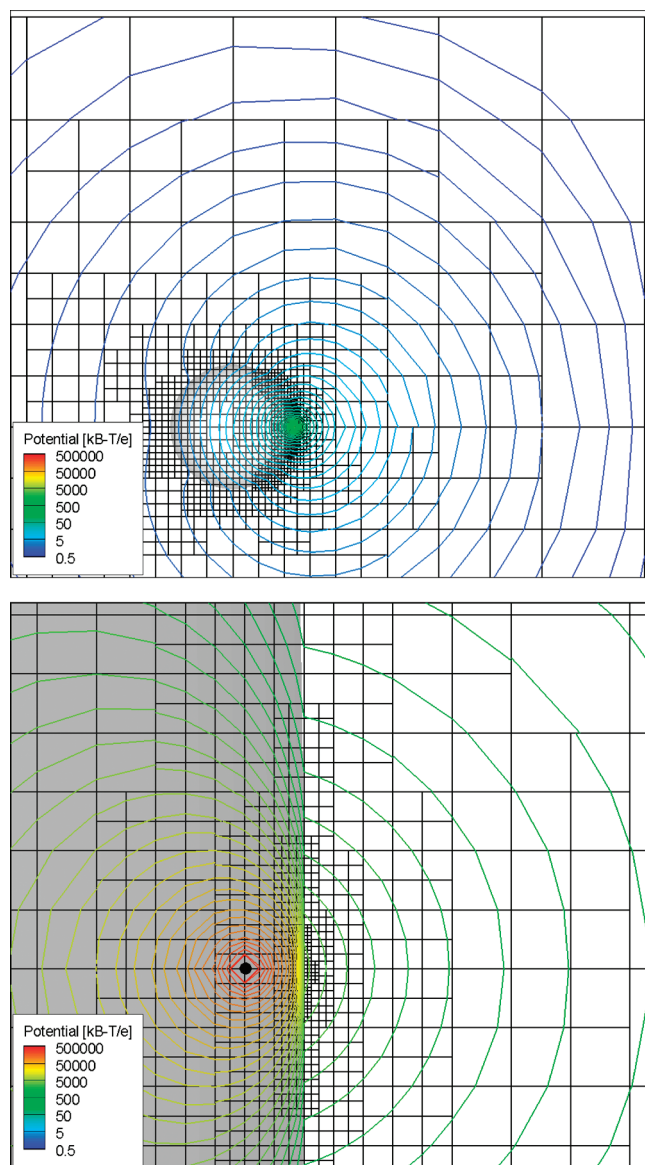


Figure 2. Cut through ACG for unit charge placed at $\rho = 0.9969i$ inside a low dielectric spherical cavity. The lower graph provides a closeup of the mesh and solution near the charge site inside the low dielectric spherical cavity.

field electrostatic potential vary most rapidly. The rapid variation in the solution about the charge reflected in the contours is due to the analytically evaluated Coulombic potential contribution. Both outside and inside the molecule the potential maps are smooth and well-behaved, including near the unit charge placed inside the low dielectric sphere.

The numerical error defined as given by $E_{\text{rf}} = G_{\text{rf}}^{\text{comp}} / G_{\text{rf}}^{\text{exact}} - 1$ is plotted as a function of distance below the surface in Figure 3 and shows that the error remains small even when the charge comes very close to the surface. For charges located within 99% of the spherical cavity radius, errors remain 1% or less.

Nonlinear PBE for a Low Dielectric Spherical Cavity of Varying Central Charge in a Salt Solution. The nonlinear behavior of a spherical cavity containing a centrally located charge is considered to verify accurate recovery of nonlinear solutions and demonstrate stable convergence at high net charge values. The governing PBE in this case reduces to a second order ordinary

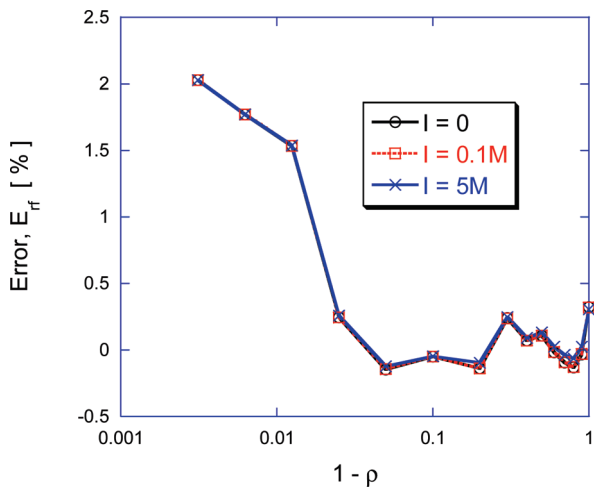


Figure 3. Error, $E_{rf} = G_{rf}^{\text{comp}}/G_{rf}^{\text{exact}} - 1$, plotted as a function of the distance of the interior unit charge, from the surface of the sphere. The linear PBE is solved over a unit radius spherical cavity with $\varepsilon_1 = 2$ and $\varepsilon_2 = 80$ under three different salt conditions: $I_{1:1} = 0, 0.1$, and 5.0 M corresponding to Debye–Hückel screening parameters, $\kappa = 0, 0.103$, and 0.728 \AA^{-1} , respectively.

differential equation (ODE) that can be solved by alternative means (e.g., Appendix A of ref 11). Two cases are considered in this study. In the first, a centrally located $50e$ charge is placed inside a 20 \AA radius sphere and the 1:1 salt concentration varied. The dielectric constant inside and outside the sphere are 4 and 78.5, respectively, and the temperature of the salt solution is $T = 300 \text{ K}$. This case was examined by Zhou,⁵³ and his results closely agree with the ones obtained here. The variation of the total electrostatic free energy, G^{el} , as a function of a 1:1 salt concentration is also considered in Figure 4. According to eq 23, the slope of the G^{el} vs κ curve is related to the excess osmotic pressure energy contribution. This relationship thus constitutes an internal consistency check valid for general molecular geometries. The plot compares three different predictions of this electrostatic energy slope: (i) the right-hand side of eq 23, where the excess osmotic pressure, $\Delta\Pi$, is obtained using ACG-PBE; (ii) differentiation of a piecewise quadratic fit to the $G^{\text{el}} \sim \kappa$ curve where G^{el} is obtained from ACG-PBE; and (iii) the excess osmotic pressure predicted using the 1D analysis.¹¹ Close agreement is established over the entire 1:1 salt concentration range. The minor departure at the highest salt concentration appears to be due to the finite differencing algorithm, the excess osmotic pressure energy contributions obtained with the 1D solver, and ACG-PBE remaining in close agreement.

Next, the net charge is increased from $1e$, where the PBE solution is essentially linear, to $10\,000e$, where nonlinear behavior dominates and the ability of the ACG solver to converge the solution in a robust manner is put to the test. In all cases, the number of multigrid cycles required to converge the solution ranged between 40 and 60. Figure 5 records the electrostatic free energy contributions, normalized by G_f for the linear problem, $G_f(\text{lin})$. Note that $G_f(\text{lin})$ can be expressed analytically, and the resulting values are in close agreement with the numerical predictions. Normalizing the electrostatic free energy contributions this way highlights the relative importance of the various nonlinear contributions. Again, good agreement between the 1D and ACG PB results is obtained. The change in normalized fixed charge energy, $\Delta G_f/G_f(\text{lin})$ (here, $\Delta G_f = G_f - G_f(\text{lin})$ and $G_f = G_{rf}$), is

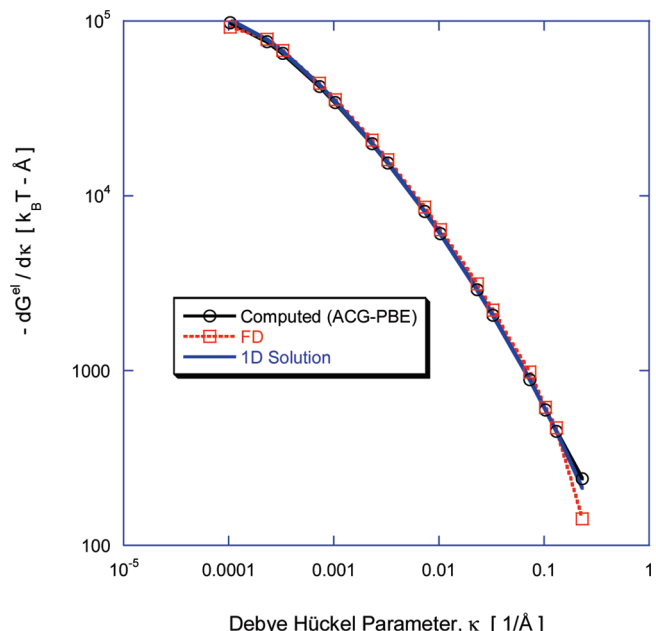


Figure 4. Comparison of salt sensitivity, $\partial G^{\text{el}}/\partial \kappa$, obtained from (i) the osmotic pressure, $\Delta\Pi$, computed with the ACG-PBE solver and relation 23; (ii) finite differencing of the G^{el} vs κ curve obtained with the ACG-PBE solver; and (iii) a 1D high resolution calculation. Nonlinear energy contributions as a function of the Debye–Hückel parameter, κ , for the single centrally located charge of $50e$ inside a 20 \AA radius sphere. The dielectric constants are $\varepsilon_1 = 4$ and $\varepsilon_2 = 78.5$.

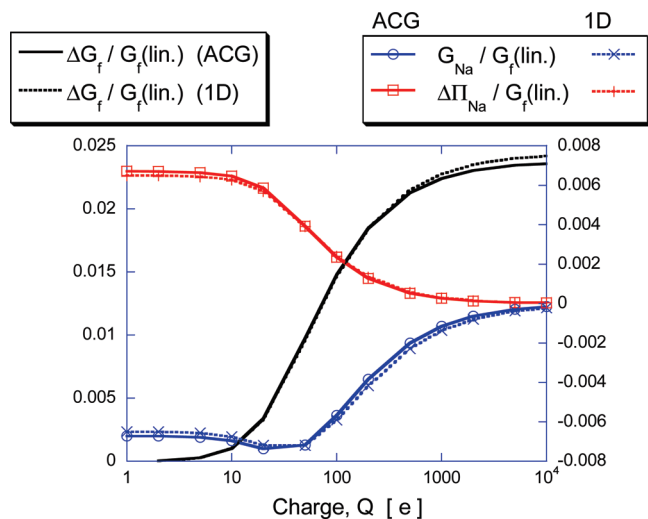


Figure 5. Charge dependence of electrostatic free energy ratios for $I = 0.03 \text{ M}$. Results are obtained using the ACG scheme and the 1D finite element solution for the case of a spherical cavity with centrally located charge. The plotted electrostatic free energies, $\Delta G_f = G_f - G_f(\text{lin})$, G_{Na} , and $\Delta\Pi_{Na}$, are normalized by the fixed charge energy obtained from the linear PBE, $G_f(\text{lin})$. In this case, this equals the reaction field energy, G_{rf} since the Coulombic energy is zero.

seen to be negligible at small charge values but to dominate the nonlinear contributions at higher charge values. Also, $\Delta G_f/G_f(\text{lin})$ seems to asymptote to a constant value at very high net charges. The opposite trend holds for the other two normalized electrostatic free energy contributions, $G_{Na}/G_f(\text{lin})$ and $\Delta\Pi_{Na}/G_f(\text{lin})$,

which individually contribute a fixed fraction of total electrostatic energy at the low charge range. As net charge increases, however, their relative contributions diminish to zero. Also, since these two electrostatic free energy terms have opposite sign, their combined contribution is quite small over the entire charge range.

Electrostatic Interaction Free Energies for Two Low Dielectric Charged Spherical Cavities Embedded in an Aqueous Salt Medium. The long-range and nonspecific electrostatic interactions can modulate the kinetic rates of association of protein–protein and protein–nucleic acid association processes.⁵⁴ For instance, changes in the ionic conditions and charge distribution of the binding partners have a significant impact on the kinetic association rates of various biomolecular complexes.^{55,56} The quantity of interest here is the electrostatic interaction free energy, which is the difference between the total electrostatic free energy of the complex and the summed total electrostatic energies of the individual molecules considered in isolation. Simple model two low dielectric spherical cavity systems have been studied previously using semianalytical treatments and are useful for validation purposes.⁵⁷ Electrostatic interaction or binding free energies can be difficult to calculate because they are usually much smaller in magnitude than the quantities being differenced. Therefore, the effects of truncation and other discretization errors upon the electrostatic interaction energy may be much more pronounced than for the total electrostatic energies of the two interacting partners.

Accurate electrostatic binding free energies for realistic and large-scale biomolecular systems are given below and elsewhere using the ACG PBE solver.^{58–62} Here, the electrostatic interaction between a pair of low dielectric spherical cavities, containing interior charges, is considered as a model problem for verifying the ability to accurately calculate these interaction energies. The first sphere has a radius of 14 Å and contains three interior charges, $\{Q_i\} = \{-2.29, +8, +2.29\}e$, distributed along the x axis at locations $x_i = \{-7.8, 0, +7.8\}$ Å, relative to the center. The second sphere has a radius of 21 Å and also contains three interior charges, $\{Q_i\} = \{-2.21, -12, +2.21\}e$, distributed along the x axis at locations $x_i = \{X_2 - 11.7, X_2, X_2 + 11.7\}$ Å, where the separation, X_2 , is the x location of the second sphere center. The dielectric constants chosen for this example are $\epsilon_{in} = 4$ and $\epsilon_{out} = 78.5$. The Debye–Hückel screening parameter $\kappa = 0.1316 \text{ \AA}^{-1}$.

Figure 6 compares the electrostatic interaction free energy obtained using the ACG PBE solver with semianalytical predictions⁵⁷ demonstrating excellent agreement when the same (van der Waals) surface is used to define the solute boundary that separates the interior and exterior dielectric regions. The total electrostatic free energies of the isolated 14 Å and 21 Å low dielectric charged spheres are -199.3 and -283.2 kcal/mol, respectively. Hence, the electrostatic interaction free energy is 2 orders of magnitude smaller than the individual electrostatic free energies. As one would expect, the choice of molecular surface affects the computed electrostatic interaction energy when spheres are closer than the solvent probe diameter (2.8 Å). Figure 6 also compares the electrostatic interaction energy obtained using the solvent excluded molecular surface. The resulting curve deviates significantly from the one using the van der Waals surface with a factor of 4 difference being obtained at the 35 Å separation.

High Resolution Surface Potential Maps of Nucleic Acids and Their Binding Partners. Surface potential maps are now routinely used to identify potential binding or recognition sites on biomolecules at atomic resolution. For example, unique

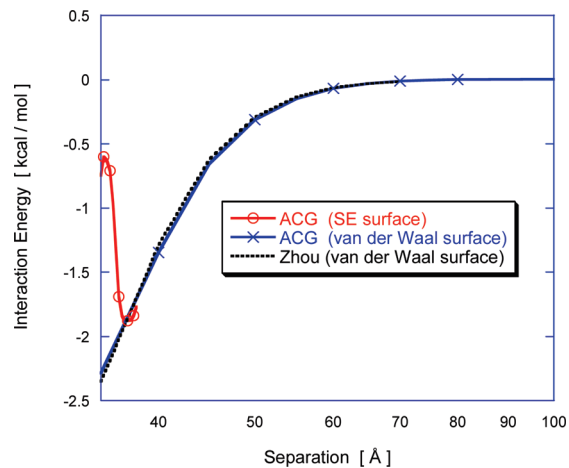


Figure 6. Electrostatic interaction energy for two low dielectric spherical cavities with interior charges embedded in a high dielectric ionic solvent, as a function of separation distance between the centers of the charged spherical cavities.

recognition or ion binding sites in irregular RNA structures, that contain noncanonical base pairs (e.g., GU wobble base pairs) and/or extruded (non)canonical bases, have been identified using the hybrid boundary element and finite difference nonlinear PB solver¹¹ and confirmed using the ACG-PB technology.^{63,64} Obtaining such quantitative or high resolution electrostatic potential maps of large-scale biomolecules—especially highly charged ones like nucleic acids and their complexes with various charged binding partners—is very challenging for any PB solver. Surface potential maps are generated for three configurations: a small, low-charge RNA binding protein along with a single-stranded (ss) RNA binding partner, and a more highly charged noncanonical DNA structure using the nonlinear form of the PBE. The first case examines the binding of the cationic Fox-1 protein (net charge = $+3e$) to the RNA element UGCAUG (PDB id: 2err, model 1), where the latter is a simple single-stranded RNA structure. The solute boundary is modeled using the solvent excluded surface with atomic radii and charges specified using the CHARMM27 force field parameters.³⁸ As previously, the ion exclusion region is omitted; also $T = 298 \text{ K}$, $\epsilon_1 = 2$, and $\epsilon_2 = 80$. The surface mesh spacing resolution is set to 0.3 \AA and the outer boundary set to approximately 3 times the largest molecule dimension. In this study, the first model of the NMR ensemble was employed to assess the error incurred in electrostatic potential calculations. The histidine residues were considered unprotonated, while other charged residues were assigned protonation states based on a physiological pH value of 7. Thus, the Asp and Glu residues had a charge of $-1e$, whereas a charge of $+1e$ was assigned to the Lys and Arg residues. The 1:1 (i.e., NaCl) salt concentration was fixed at 0.1 M.

The surface maps are obtained by first identifying the mesh edges intersected by the surface (i.e., those edges with an end point in the interior and exterior domains) and then calculating the intersection points. A triangulation of the intersection points is then developed and the potentials at the intersection points developed by extrapolating the ACG solution to the surface using the nearest exterior mesh nodes. All surface potential maps are are produced using the commercial program, TecPlot.

As evident from Figure 7a,b, the single RNA element lies in a distinct pocket of very positive electrostatic potential on the RNA

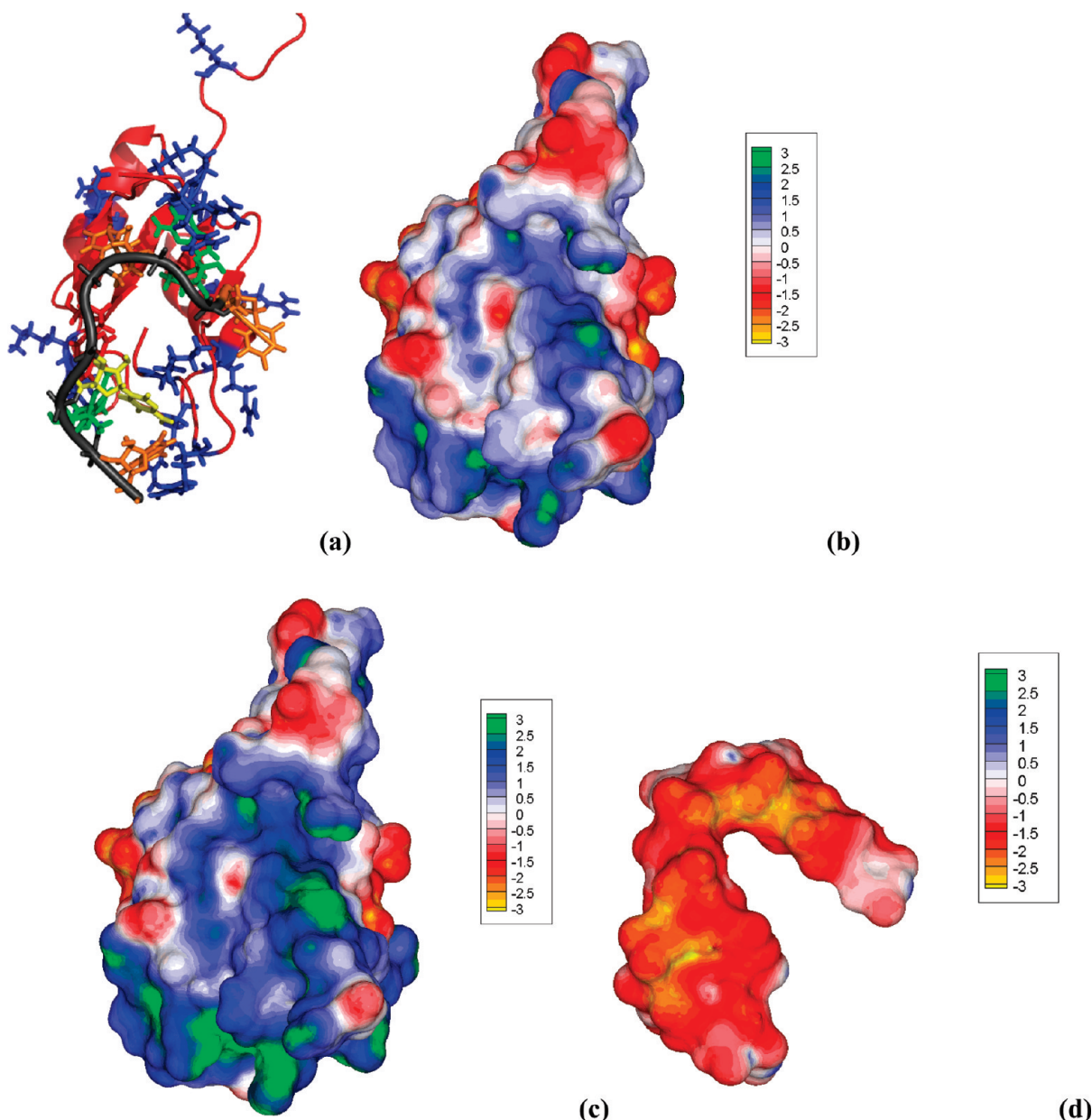


Figure 7. Different depictions of the NMR structure of RNA binding domain (RBD) of Fox-1 in complex with the single-stranded UGCAUGU RNA element (PDB id: 2err, model 1). (a) RNA phosphate backbone depicted by the dark gray ribbon and the different bases colored as adenine = red, uracil = orange, guanine = green, and cytosine = yellow. The protein peptide backbone adopts an orange ribbon representation with positively and negatively charged side chains shown as blue and red sticks, respectively. This view emphasizes the clustering of various cationic protein residues at the RNA binding interface. (b) Surface electrostatic potential (in kcal/mol/e) and overall shape of the RBD of Fox-1. A well-defined and concave region of positive potential, generated by the cationic protein residues and traced by the bent RNA structure, is clearly shown when the nonlinear PBE solution is employed. This cationic protein (net charge = +3e) follows the electrostatic pattern of other RNA binding proteins that have a distinct positive potential patch on their binding interface.⁷⁸ Thus, the RNA fills most of the concave blue/green protein surface to which it is complementary in both shape and electrostatic potential. (c) Same view and color map as b but using the linear PBE. The positive electrostatic potential is now overestimated and the positive region much broader than in b. (d) Electrostatic potential of the single-stranded bent and overall negatively charged RNA structure. As expected, an overall negative potential covers most of the RNA surface due to the presence of the anionic phosphate groups.

binding domain of the Fox-1 protein. It has been previously reported^{65,66}—on the basis of linear PBE evaluations—that the surface potential in the RNA binding site of this protein is neutral. However, this is not borne out by the results obtained here with the nonlinear PBE (Figure 7b), thus highlighting the drawbacks of forming conclusions on the basis of linear PBE calculations. Predictions using the linear ACG-PB solver also show a significantly different surface potential distribution for the

protein RNA binding domain of Fox-1 relative to the nonlinear one (see Figure 7b,c). The electrostatic potential of the ssRNA is negative over most of its surface (Figure 7d), whereas the negative potential regions of the RNA are attenuated with the presence of the cationic protein (results not shown).

The second example is the deformed and nonlinear DNA structure in association with the Tc3 transposase protein (PDB id: 1tc3). Charges and radii are assigned using the AMBER force

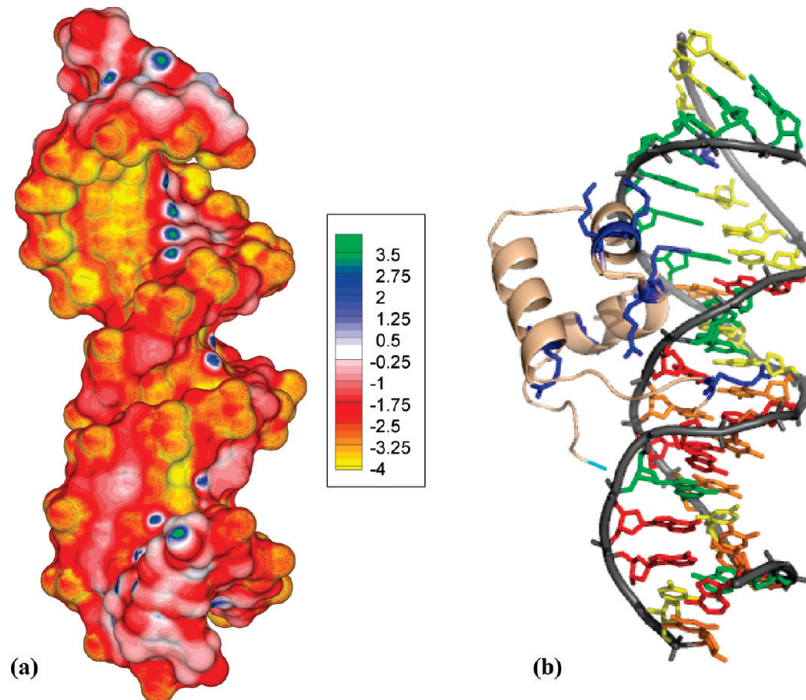


Figure 8. (a) The surface potential of the deformed and nonlinear DNA. Radii and atomic charges are assigned using the Amber force field. This unique A/B junction DNA structure generates a surface potential map with characteristics of an A-DNA major groove and B-DNA minor groove. A continuous high negative potential band along the G stretch along with electropositive spots due to amino groups of cytosine is observed for this nonlinear DNA structure. The electrostatic potential is given in units of kcal/mol/e. (b) The N-terminal DNA-binding domain of Tc3 transposase bound to the DNA (PDB id: 1TC3). The ribbon or tube-like representation of the DNA phosphate backbone is shown in light gray and that of the peptide backbone in gold. The bases are colored as adenine = red, thymine = orange, guanine = green and cytosine = yellow. The cationic residues that penetrate in the narrow minor groove or face the G-stretch side of the major groove are shown in blue stick representation.

field,³⁷ and the solute boundary is represented using the solvent excluded molecular surface. Also, $T = 298\text{ K}$, $\epsilon_1 = 2$, and $\epsilon_2 = 80$. The 1:1 salt concentration is set to 0.1 M. It is desirable that the electrostatic potential maps for nucleic acids capture unique local sequence dependent features and the intricate phosphate charge distribution (e.g., close clustering of phosphate groups that occurs at helical junctions in RNA and DNA structures). Here, high resolution surface potential maps capturing these features are produced. As portrayed in Figure 8a, the G stretch of the major groove side of the DNA structure and its locally narrowed minor groove have a deep negative potential.⁶⁷ The extensive region of negative potential along the G stretch of the major groove is mostly due to the deformation of the DNA structure. Figure 8b shows how the protein Tc3 transposase positions several positively charged side chains along one side of the major groove and in the narrow minor groove, forming numerous hydrogen bonds and salt bridges in these grooves. The linear PB solution produces much larger and more negative potential patches on the grooves (results not shown).

High Resolution Surface Electrostatic Potential Maps of Large-Scale Biomolecular Assemblies: Ribosomes. Due to the large-scale and highly charged nature of biomolecular assemblies such as ribosomes, which can contain more than a million atoms, it is very challenging to obtain stable and accurate electrostatic properties with standard 3D lattice nonlinear PB solvers. To date, these calculations require access to supercomputers and special techniques such as parallel focusing.^{14,68} Moreover, these calculations often encounter convergence issues when using the nonlinear PBE necessary to properly model these highly charged systems at the all-atom level and for resolutions finer than 0.6 Å.^{69–72}

The computation of the surface potential can be computationally demanding for the large-scale biomolecular assemblies here considered, making such computations inaccessible to desktop computers and even large clusters. Thus, to the best of our knowledge, the results here shown represent the first nonlinear PB calculation done on a serial platform for such a large-scale biomolecular system at a level of fine grid resolution of 0.3 Å using an all-atom model of a ribosomal subunit. All other reported surface potential maps of large-scale biomolecular assemblies, such as the small 30S ribosomal subunit or viruses, that were done using serial computers were obtained with the linear PBE solution, coarser grid resolutions, or more approximate generalized Born-based approaches.^{3,69–76}

Here, a high resolution electrostatic potential map of the large 50S ribosomal subunit structure from *H. marismortui* (PDB id: 3cc4) was computed using the nonlinear PBE. This large ribosomal subunit consists of 5S and 23S RNA and numerous proteins with 150 970 atoms and has a net charge of $-2949e$ (see Figure 9a). The cocrystal structure of anisomycin bound to the 50S ribosomal subunit was taken from the RCSB PDB Databank. All cofactors including metals and drugs were removed from the structure and only the protein and RNA chains retained. The CHARMM³⁸ force field atomic radii and charges were used for these PB calculations after the missing hydrogen atoms were added to the structure using the pdb2pqr server.⁷⁷ The 1:1 salt concentration was 0.1 M ($\kappa = 0.1030\text{ \AA}^{-1}$), and the dielectric constants ϵ_1 and ϵ_2 were 2 and 80, respectively.

Using a finest mesh spacing of 0.3 Å results in an ACG mesh with a total of 52.5 million nodes. Meshing the minimum enclosing

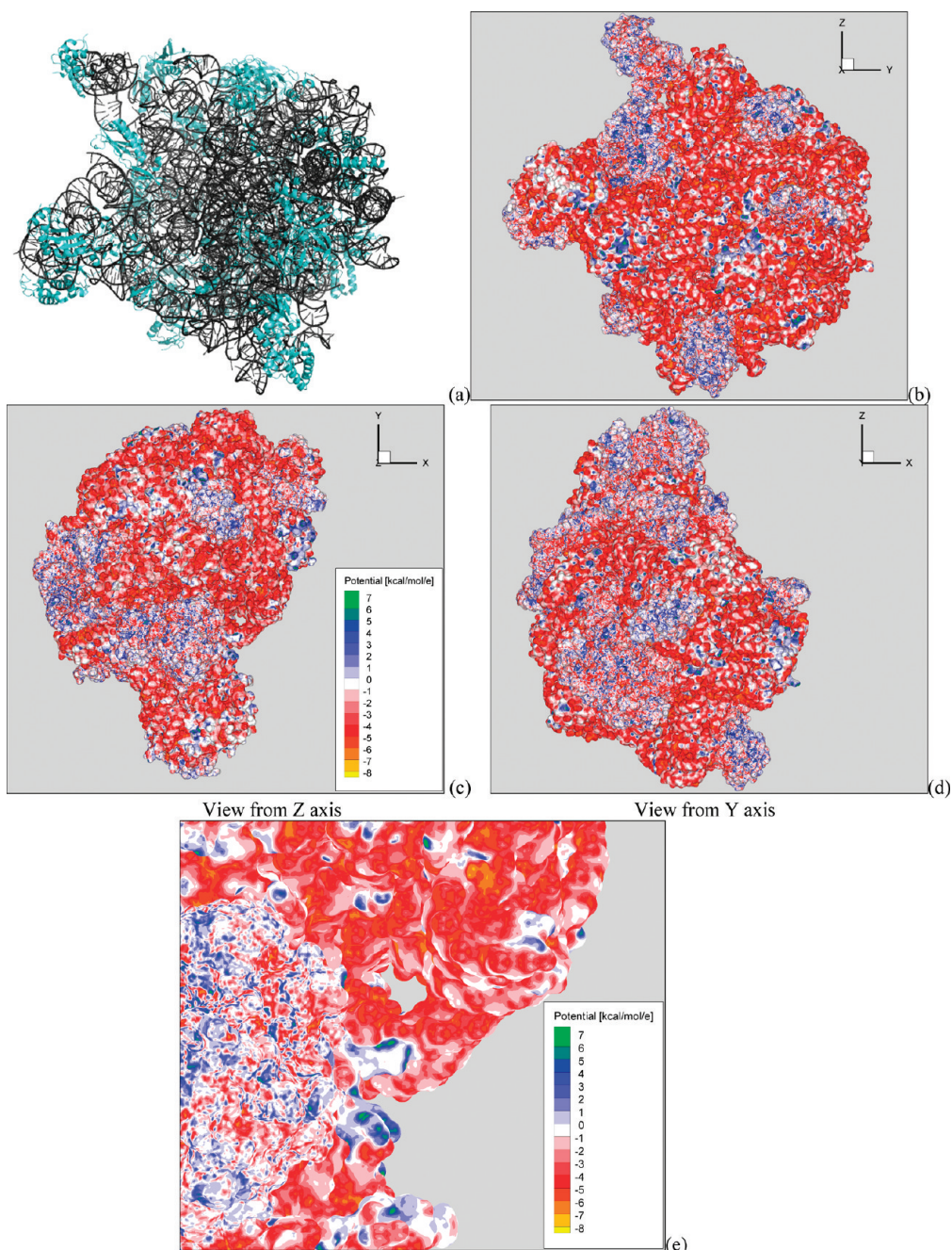


Figure 9. (a) Ribbon representation of the 50S ribosomal subunit (PDB id: 3cc4; net charge: $-2949e$; 150 970 atoms). The protein and rRNA molecules are shown in cyan and dark gray, respectively. (b–d) Different views of the surface potential (in kcal/mol/e) of the whole 50S ribosomal subunit. Note that the red and blue patches correspond to regions where the RNA and protein lie, respectively. (e) Closeup view of a particular intricate region of the complex 50S subunit showing the high quality of the generated surface potential map using the ACG nonlinear PB solver at the required mesh spacing to resolve the surface geometry.

box using a regular lattice grid with the same finest spacing would require 354 million nodes. Here, the outer boundary side length is 3 times larger than the longest molecular dimension, and thus the complete mesh spans 1228 Å. Solving the nonlinear PBE for this configuration produces stable and converged results within 170 iterations. With the ACG-based PBE solver, the nonlinear PBE solution for this large-scale and highly charged biomolecular assembly took 13.5 h using a 10-node 64-bit SGI Altix workstation. Machines of this caliber are widespread in university research departments

and small businesses conducting computational biophysics research.

Figure 9b–d shows the electrostatic potential maps for the 50S ribosomal subunit (PDB id: 1CC4) and viewed from z , y , and x axes. The regions of positive and negative potential on the molecular surface correspond to the locations of the proteins and RNA, respectively. The presence of the proteins is essential in order to neutralize the close repulsive phosphate–phosphate interactions and thus help stabilize this intricate large-scale protein–RNA complex. A closeup of a portion of the surface

potential in Figure 9e reveals the resolution and attendant quality of the surface potential map. The linear PB solution provides a different potential distribution on the surface of this highly charged biomolecular entity (results not shown). Thus, the nonlinear Poisson–Boltzmann solution should be used when modeling nonspecific electrostatic interactions of the ribosome, its assembly process, and associations with charged drug ligands.

■ CONCLUDING REMARKS AND FUTURE DIRECTIONS

A finite difference method to solve the linear/nonlinear Poisson–Boltzmann equation has been formulated and implemented on the grid structure known as an adaptive Cartesian mesh or octree. The generation of the mesh about a biomolecular structure, the construction of the finite difference operators upon the mesh, the representation of the electrostatic potential inside and outside the molecular surface, and preliminary computational results have been presented in this paper. Properties and advantages of the ACG-based PBE approach include the following:

- fast mesh generation due to the simple fundamental shape of the ACG cells
- optimized grid spacing where fine cells are used where the potential gradients are changing most rapidly (i.e., at the surface) and coarser elements used elsewhere
- use of compact finite difference formulas to evaluate the dielectric-weighted Laplacian and tailored for implementation on the ACG
- a representation of the potential (total potential outside the molecule and reaction field potential inside), which completely eliminates charge singularities and numerically induced self-charging energies
- a robust multigrid-accelerated convergence scheme
- the incorporation of a recently developed outer boundary treatment to estimate the boundary potential and provide first-order (i.e., based on a monopole approximation) corrections to computed energies.

Application of the method to idealized configurations involving charged and low dielectric spheres embedded in a high dielectric ionic solvent has confirmed that the method successfully maintains high accuracy as a charge is placed near the surface, properly predicts the electrostatic interaction energies for a pair of charged spheres, and reliably converges solutions for very highly charged systems. Comparisons with semianalytical solutions to the nonlinear PBE have verified that the ACG-based method accurately reproduces the salt-dependent behavior of highly charged spheres immersed in 1:1 salt solutions. PB calculations involving very complex biomolecular systems involving highly charged nucleic acid assemblies including the 50S ribosomal subunit have also been carried out successfully. The ACG-PB solver in conjunction with molecular dynamics or Brownian dynamics techniques should allow more careful and systematic studies of the role of nonspecific electrostatic interactions on the binding of various antibacterial drugs to the ribosome and ribosome and virus assembly processes at atomic resolution. An assessment of the performance of the nonlinear and linear PB predictions of electrostatic solvation free energies for a test set of 55 proteins—that vary in size, shape, and charge distribution—is also provided in order to establish benchmark test cases for comparisons with other PB solvers.

Ongoing activity in the development of the ACG-based PBE solver includes improved treatment of the solution near the

dielectric interface to obtain more accurate predictions of the surface potential and normal gradients and, hence, forces; incorporation of nonuniform ion size effects; the calculation of electrostatic interaction energies between the two molecules where the bound and unbound states differ; and validation/testing of all of the above new ACG-PB features for a variety of biomolecular systems.

■ ASSOCIATED CONTENT

S Supporting Information. Electrostatic free energies and its salt sensitivities for a set of 55 proteins based on the linear and nonlinear ACG-PB solution. This material is available free of charge via the Internet at <http://pubs.acs.org>.

■ AUTHOR INFORMATION

Corresponding Author

*E-mail: alex@continuum-dynamics.com; mfenley@sb.fsu.edu.

■ ACKNOWLEDGMENT

This work has been supported by the NIH under Grant numbers 5 R44 GM57764-03 and 5R44GM073391-03 with technical monitors, Dr. Janna Wehrle and Jeni Smits. The content is solely the responsibility of the authors and does not necessarily represent the official views of the National Institute of General Medical Sciences or the National Institutes of Health. One of the authors (M.O.F.) acknowledges the support from NIH-GM07838-01 (PI: Dr. Michael S. Chapman, OHSU, Co-PI: Dr. Marcia O. Fenley). One of the authors (M.O.F.) would like to thank Dr. Cristina Russo, Mr. Travis Mackoy, and Mr. Robert Harris for help in preparing structures, figures, and some PB calculations.

■ NOMENCLATURE

C = energy conversion factor, as defined in eq 22

e = protonic charge

$f(\Phi)$ = mobile ion charge function, as defined in eq 12

G^{el} = total electrostatic free energy, as defined in eq 20

G_f = fixed charged energy contribution, as defined in eq 21a

G_m = dielectric stress energy contribution, as defined in eq 21b

G_{rf} = reaction field energy, as defined in eq 24

$\mathbf{i}, \mathbf{j}, \mathbf{k}$ = unit vectors along x , y , and z , respectively

$I_{1:1}$ = ionic strength of the 1:1 (monovalent) salt

k_B = Boltzmann constant

M' = /th level mesh in multigrid scheme (M^0 is the finest level mesh)

q_k = normalized charge, $q_k = (4\pi e/\epsilon_1 k_B T)Q_k$, where ϵ_1 is the interior dielectric constant

Q_k = value of the k th charge, in units of e (electron charge)

\mathbf{R}_i = position of the i th node in the ACG mesh

t = Stern layer or ion-exclusion thickness, in Å

T = absolute temperature of the aqueous salt solution, in K

$\delta(\mathbf{r})$ = 3D Dirac δ function centered at $\mathbf{r} = \mathbf{0}$

Δ_i = size (side length) of the i th mesh cell

$\Delta\Pi$ = excess osmotic pressure energy, as defined in eq 21c

ϵ = dielectric constant

ϵ_1, ϵ_2 = dielectric constant in the interior (Ω_1) and exterior (Ω_2 and Ω_3) regions, respectively

Φ = reduced (or dimensionless) total electrostatic potential

Φ^c = Coulombic potential, as defined in eq 14

Φ^g = potential field computed on the ACG grid and defined in eq 16
 Φ^{rf} = reaction field potential, $\Phi^{rf} = \Phi - \Phi^c$
 κ = Debye–Hückel screening parameter, as defined in eq 11, in Å⁻¹
 λ_i = residual, as defined in eq 18
 ρ = charge density, in e/Å³
 ρ^f = contribution of fixed solute charges to the total charge density, in e/Å³
 ρ^m = contribution of mobile ions to the total charge density, in e/Å³
 ρ_k = position of k th charge
 σ_i = Coulombic source term
 ω_{ij} = weights in the discrete approximation to the weighted Laplacian, e.g., eq 17
 Ω_i = volume domains corresponding to the molecule interior (Ω_1), the Stern layer (Ω_3), and the remaining region, $\Omega_2 = R^3 - \Omega_1 - \Omega_3$
ACG = adaptive Cartesian grid
ACG-PBE = ACG-based PBE solver
BEM = boundary element method
FD = finite difference
FE = finite element
PBE = Poisson–Boltzmann equation
PDB = Protein Data Bank
PDE = partial differential equation
SE = solvent-excluded (surface)
vdW = van der Waals (surface)

■ REFERENCES

- (1) Lu, B.; Zhou, Y. C.; Holst, M. J.; McCammon, J. A. Recent progress in numerical methods for the Poisson–Boltzmann equation in biophysical applications. *Commun. Comput. Phys.* **2008**, *3*, 973–1009.
- (2) Lu, J.; Deutsch, C. Electrostatics in the Ribosomal Tunnel Modulates Chain Elongation Rates. *J. Mol. Biol.* **2008**, *384*, 73–86.
- (3) Zhang, D.; Konecny, R.; Baker, N. A.; McCammon, J. A. Electrostatic interaction between RNA and protein capsid in cowpea chlorotic mottle virus simulated by a coarse-grain RNA model and a Monte Carlo approach. *Biopolymers* **2004**, *75*, 325–337.
- (4) Boschitsch, A. H.; Fenley, M. O.; Zhou, H.-X. Fast Boundary Element Method for the Linear Poisson–Boltzmann Equation. *J. Phys. Chem. B* **2002**, *106*, 2741–2754.
- (5) Bharadwaj, R.; Windemuth, A.; Sridharan, S.; Honig, B.; Nicholls, A. The Fast Multipole Boundary Element Method for Molecular Electrostatics: An Optimal Approach for Large Systems. *J. Comput. Chem.* **1995**, *16*, 898–913.
- (6) Purisima, E. O. Fast Summation Boundary Element Method for Calculating Solvation Free Energies of Macromolecules. *J. Comput. Chem.* **1998**, *19*, 1494–1504.
- (7) Zauhar, R. J.; Varnek, A. A Fast and Space Efficient Boundary Element Method for Computing Electrostatic and Hydration Effects in Large Molecules. *J. Comput. Chem.* **1996**, *17*, 864–877.
- (8) Boschitsch, A. H.; Fenley, M. O.; Olson, W. K. A Fast Adaptive Multipole Algorithm for Calculating Screened Coulomb (Yukawa) Interactions. *J. Comput. Phys.* **1999**, *151*, 212–241.
- (9) Lu, B.; Cheng, X.; Huang, J.; McCammon, J. A. Order N algorithm for computation of electrostatic interactions in biomolecular systems. *Proc. Natl. Acad. Sci. U.S.A.* **2006**, *103*, 19314–19319.
- (10) Lu, B.; Cheng, X.; McCammon, J. A. “New-version-fast-multipole-method” accelerated electrostatic calculations in biomolecular systems. *J. Comput. Phys.* **2007**, *226*, 1348–1366.
- (11) Boschitsch, A. H.; Fenley, M. O. Hybrid Boundary Element and Finite Difference Method for Solving the Nonlinear Poisson–Boltzmann Equation. *J. Comput. Chem.* **2004**, *25*, 935–955.
- (12) Baker, N. A.; Holst, M. J.; Wang, F. Adaptive Multilevel Finite Element Solution of the Poisson–Boltzmann Equation II. Refinement at Solvent-Accessible surfaces in Biomolecular Systems. *J. Comput. Chem.* **2000**, *21*, 1343–1352.
- (13) Holst, M.; Baker, N.; Wang, F. Adaptive Multilevel Finite Element Solution of the Poisson–Boltzmann Equation I: Algorithms and Examples. *J. Comput. Chem.* **2000**, *21*, 1319–1342.
- (14) Baker, N. A.; Sept, D.; Joseph, S.; Holst, M. J.; McCammon, J. A. Electrostatics of Nanosystems: Application to Microtubules and the Ribosome. *Proc. Natl. Acad. Sci. U.S.A.* **2001**, *98*, 10037–10041.
- (15) Madura, J. D.; Briggs, J. M.; Wade, R. C.; Davis, M. E.; Luty, B. A.; Ilin, A.; Antosiewicz, J.; Gilson, M. K.; Bagheri, B.; Scott, L. R.; McCammon, J. A. Electrostatics and Diffusion of Molecules in Solution: Simulations with the University of Houston Brownian Dynamics Program. *Comput. Phys. Commun.* **1995**, *91*, 57–95.
- (16) Jo, S.; Vargyas, M.; Vasko-Szedlar, M.; Roux, B.; Im, B. PBEQ-Solver for online visualization of electrostatic potential of biomolecules. *Nucleic Acids Res.* **2008**, *36*, W270–W275.
- (17) Bashford, D.; Gerwert, K. Electrostatic Calculations of the pKa Values of Ionizable Groups in Bacteriorhodopsin. *J. Mol. Biol.* **1992**, *224*, 473–486.
- (18) Grant, J. A.; Pickup, B. T.; Nicholls, A. A smooth permittivity function for Poisson–Boltzmann solvation methods. *J. Comput. Chem.* **2001**, *22*, 608–640.
- (19) Gilson, M. K.; Sharp, K.; Honig, B. Calculating the electrostatic potential of molecules in solution: Method and error assessment. *J. Comput. Chem.* **1987**, *9*, 327–335.
- (20) Cai, Q.; Hsieh, M.-J.; Wang, J.; Luo, R. Performance of Non-linear Finite-Difference Poisson–Boltzmann Solvers. *J. Chem. Theory Comput.* **2010**, *6*, 203–211.
- (21) Luo, R.; David, L.; Gilson, M. K. Accelerated Poisson–Boltzmann calculations for static and dynamic systems. *J. Comput. Chem.* **2002**, *23*, 1244–1253.
- (22) Wang, J.; Luo, R. Assessment of Linear Finite-Difference Poisson–Boltzmann Solvers. *J. Comput. Chem.* **2010**, *31*, 1689–1698.
- (23) Boschitsch, A. H.; Fenley, M. O. A New Outer Boundary Formulation and Energy Corrections for the Nonlinear Poisson–Boltzmann Equation. *J. Comput. Chem.* **2007**, *28*, 909–921.
- (24) Gilson, M. K.; Sharp, K. A.; Honig, B. Calculating electrostatic interactions in biomolecules: method and error assessment. *J. Comput. Chem.* **1988**, *9*, 327–335.
- (25) Cortis, C. M.; Friesner, R. A. An Automatic Three-Dimensional Finite Element Mesh Generation System for the Poisson–Boltzmann Equation. *J. Comput. Chem.* **1997**, *18*, 1570–1590.
- (26) Bajaj, C. L.; Xu, G.; Zhang, Q. A Fast Variational Method for the Construction of Resolution Adaptive C²-Smooth Molecular Surfaces. *Comput. Methods Appl. Mech. Eng.* **2009**, *198*, 1684–1690.
- (27) Samet, H. *The Design and Analysis of Spatial Structures*; Addison-Wesley Publishing Company, Inc.: Reading, MA, 1990; p 510.
- (28) Mirzadeh, M.; Theillard, M.; Gibou, F. A second-order discretization of the nonlinear Poisson–Boltzmann equation over irregular geometries using non-graded adaptive Cartesian grids. *J. Comput. Phys.* **2011**, *230*, 2125–2140.
- (29) Aftosmis, M. J.; Berger, M. J.; Melton, J. E. Robust and Efficient Cartesian Mesh Generation for Component-Based Geometry. *AIAA J.* **1998**, *36*, 952–960.
- (30) Murman, S. M.; Aftosmis, M. J.; Berger, M. J., Simulations of Store Separation from an F/A-18 with a Cartesian Method. *J. Aircraft* **2004**, *41*, (4).
- (31) Aftosmis, M. J. *Solution Adaptive Cartesian Grid Methods for Aerodynamic Flows with Complex Geometries*; Lecture Notes 1997–02; Von Karman Institute for Fluid Dynamics: Rhode-St-Genèse, Belgium, 1997.
- (32) Aftosmis, M. J.; Berger, M. J.; Melton, J. E. Robust and Efficient Cartesian Mesh Generation for Component-Based Geometry. In *35th AIAA Aerospace Sciences Meeting & Exhibit*, AIAA-97-0196, Reno, NV, 1997; AIAA: Reston, VA, 1997.
- (33) Berger, M. J.; LeVeque, R. J. An Adaptive Cartesian Mesh Algorithm for the Euler Equations in Arbitrary Geometries. In *89-1930-CP*; AIAA: Reston, VA, 1989.

- (34) Wang, J.; Cai, Q.; Li, Z.-L.; Zhao, H.-K.; Luo, R. Achieving energy conservation in Poisson–Boltzmann molecular dynamics: Accuracy and precision with finite-difference algorithms. *Chem. Phys. Lett.* **2009**, *468*, 112–118.
- (35) Zhou, Z.; Payne, P.; Vasquez, M.; Kuhn, N.; Levitt, M. Finite-Difference Solution of the Poisson-Boltzmann Equation: Complete Elimination of Self-Energy. *J. Comput. Chem.* **1996**, *11*, 1344–1351.
- (36) Bondi, A. Van der Waals Volumes and Radii. *J. Phys. Chem.* **1964**, *68*, 441–451.
- (37) Cornell, W. D.; Cieplak, P.; Bayly, C. I.; Gould, I. R.; Merz, K.; Ferguson, D. M.; Spellmeyer, D. C.; Fox, T.; Caldwell, J. W.; Kollman, P. A. A 2nd generation force-field for simulation of proteins, nucleic-acids, and organic-molecules. *J. Am. Chem. Soc.* **1995**, *117*, 11946–11975.
- (38) Foloppe, N.; MacKerell, A. D. J. All-atom empirical force field for nucleic acids: I. Parameter optimization based on small molecule and condensed phase macromolecular target data. *J. Comput. Chem.* **2000**, *21*, 86–104.
- (39) Friedrichs, M.; Zhou, R.; Edinger, S. R.; Friesner, R. A. Poisson-Boltzmann Analytical Gradients for Molecular Modeling Calculations. *J. Phys. Chem. B* **1999**, *103*, 3057–3061.
- (40) Chan, S. L.; Purisima, E. O. Molecular surface generation using marching tetrahedra. *J. Comput. Chem.* **1998**, *19*, 1268–1277.
- (41) Protter, M.; Weinberger, H. F. *Maximum Principles in Differential Equations*; Prentice Hall: Englewood Cliffs, NJ, 1967; reprint by Springer-Verlag: New York, 1984.
- (42) Barth, T. J. Numerical Aspects of Computing Viscous High Reynolds Number Flows on Unstructured Meshes. In *29th Aerospace Sciences Meeting*, AIAA-91-0721, Reno, NV, 1991; AIAA: Reston, VA, 1991.
- (43) Chen, S.-W. W.; Honig, B. Monovalent and Divalent Salt Effects on Electrostatic Free Energies Defined by the Nonlinear Poisson-Boltzmann Equation: Application to DNA Binding Reactions. *J. Phys. Chem. B* **1997**, *101*, 9113–9118.
- (44) Greengard, L.; Huang, J. *A New Version of the Fast Multipole Method for Screened Coulomb Interactions in Three Dimensions*, 01-002; Courant Mathematics and Computing Laboratory, Courant Institute: New York, 2001; p 18.
- (45) Press, W. H.; Teukolsky, S. A.; Vetterling, W. T.; Flannery, B. P. *Numerical Recipes*, 2nd ed.; Cambridge University Press: Cambridge, U. K., 1992; p 960.
- (46) Holst, M.; Saied, F. Multigrid Solution of the Poisson-Boltzmann Equation. *J. Comput. Chem.* **1993**, *14*, 105–113.
- (47) Oberoi, H.; Allewell, N. M. Multigrid Solution of the Nonlinear Poisson-Boltzmann Equation and Calculation of Titration Curves. *Biophys. J.* **1993**, *65*, 48–55.
- (48) Sharp, K.; Honig, B. Calculating total electrostatic energies with the nonlinear Poisson-Boltzmann equation. *J. Phys. Chem.* **1990**, *94*, 7684–7692.
- (49) Sharp, K. A. Polyelectrolyte Electrostatics: Salt Dependence, Entropic, and Enthalpic Contributions to Free Energy in the Nonlinear Poisson-Boltzmann Model. *Biopolymers* **1995**, *36*, 227–243.
- (50) Sharp, K. A.; Friedman, R. A.; Misra, V.; Hecht, J.; Honig, B. Salt Effects on Polyelectrolyte-Ligand Binding: Comparison of Poisson-Boltzmann, and Limiting Law/Counterion Binding Models. *Biopolymers* **1995**, *36*, 245–262.
- (51) Kirkwood, J. G. Theory of Solutions of Molecules Containing Widely Separated Charges with Special Applications to Zwitterions. *J. Chem. Phys.* **1934**, *2*, 351–361.
- (52) Sader, J. E.; Lenhoff, A. M. Electrical Double-Layer Interaction between Heterogeneously Charged Colloidal Particles: A Superposition Formulation. *J. Colloid Interface Sci.* **1998**, *201*, 233–243.
- (53) Zhou, H.-X. Macromolecular Electrostatic Energy Within the Nonlinear Poisson-Boltzmann Equation. *J. Chem. Phys.* **1994**, *100*, 3152–3162.
- (54) Schreiber, G.; Haran, G.; Zhou, H.-X. Fundamental aspects of protein-protein association kinetics. *Chem. Rev.* **2009**, *109*, 839–860.
- (55) Getzoff, E. D.; Cabelli, D. E.; Fisher, C. L.; Parge, H. E.; Viezzoli, M. S.; Banci, L.; Hallewell, R. A. Faster superoxide dismutase mutants designed by enhancing electrostatic guidance. *Nature* **1992**, *358*, 347–351.
- (56) Lago, H.; Parrott, A. M.; Moss, T.; Stonehouse, N. J.; Stockley, P. G. Probing the kinetics of formation of the bacteriophage MS2 translational operator complex: identification of a protein conformer unable to bind RNA. *J. Mol. Biol.* **2001**, *305*, 1131–1144.
- (57) Zhou, H.-X. Boundary Element Solution to Macromolecular Electrostatics: Interaction energy between two proteins. *Biophys. J.* **1993**, *65*, 955–963.
- (58) Bredenberg, J.; Boschitsch, A. H.; Fenley, M. O. The role of anionic protein residues on the salt dependence of the binding of aminoacyl-tRNA synthetases to tRNA: A Poisson-Boltzmann analysis. *Commun. Comput. Phys.* **2008**, *3*, 1051–1070.
- (59) Bredenberg, J. H.; Russo, C.; Fenley, M. O. Salt-mediated electrostatics in the association of TATA binding proteins to DNA: A combined molecular mechanics/Poisson-Boltzmann study. *Biophys. J.* **2008**, *94*, 4634–4645.
- (60) Bredenberg, J. H.; Fenley, M. O. Salt dependent association of novel mutants of TATA-binding proteins to DNA: Predictions from theory and experiments. *Commun. Comput. Phys.* **2008**, *3*, 1132–1153.
- (61) Fenley, M. O.; Harris, R. C.; Jayaram, B.; Boschitsch, A. H. Revisiting the association of cationic groove-binding drugs to DNA using a Poisson-Boltzmann approach. *Biophys. J.* **2010**, *99*, 879–886.
- (62) Harris, R. C.; Bredenberg, J. H.; Silalahi, A. R. J.; Boschitsch, A. H.; Fenley, M. O. Understanding the physical basis of the salt dependence of the electrostatic binding free energy of mutated charged ligand-nucleic acid complexes. *Biophys. Chem.* **2011**.
- (63) Xu, D.; Greenbaum, N. L.; Fenley, M. O. Recognition of the spliceosomal branch site RNA helix on the basis of surface and electrostatic features. *Nucleic Acids Res.* **2005**, *33*, 1154–1161.
- (64) Xu, D.; Landon, T.; Greenbaum, N. L.; Fenley, M. O. The electrostatic characteristics of G·U wobble base pairs. *Nucleic Acids Res.* **2007**, *35*, 3836–3847.
- (65) Auweter, S. D.; Fasan, R.; Reymond, L.; Underwood, J. G.; Black, D. L.; Pitsch, S.; Allain, F., H.-T. Molecular Basis of RNA Recognition by the Human Alternative Splicing Factor Fox-1. *EMBO J.* **2006**, *25*, 163–173.
- (66) Auweter, S. D.; Oberstrass, F. C.; Allain, F., H.-T. Sequence-specific Binding of Single-stranded RNA: Is there a Code for Recognition? *Nucleic Acids Res.* **2006**, *34*, 4943–4959.
- (67) Xu, D. *Electrostatics of Nucleic Acids and Hydration Properties of the Pseudouridine Dependent Spliceosomal Branch Site Helix*; Florida State University: Tallahassee, FL, 2007.
- (68) Sayyed-Ahmad, A.; Miao, Y.; Ortoleva, P. Poisson-Boltzmann theory of bionanosystems. *Commun. Comput. Phys.* **2008**, *3*, 1100–1116.
- (69) Trylska, J.; Konecny, R.; Tama, F.; Brooks, C. L. I.; McCammon, J. A. Ribosome motions modulate electrostatic properties. *Biopolymers* **2004**, *74*, 423–431.
- (70) Trylska, J.; McCammon, J. A.; Brooks, C. L. I. Exploring Assembly Energetics of the 30S Ribosomal Subunit Using an Implicit Solvent Approach. *J. Am. Chem. Soc.* **2005**, *127*, 11125–11133.
- (71) Devkota, B.; Petrov, A.; Lemieux, S.; Bpz, M. B.; Tang, L.; Schneemann, A.; Jonhson, J. E.; Harvey, S. C. Structural and Electrostatic Characterization of Pariacoto Virus: Implications for Viral Assembly. *Biopolymers* **2009**, *91*, 530–538.
- (72) Drugosz, M.; Trylska, J. Aminoglycoside association pathways with the 30S ribosomal subunit. *J. Phys. Chem. B* **2009**, *113*, 7322–7330.
- (73) Qin, S.; Zhou, H.-X. Dissection of the High Rate Constant for the Binding of a Ribotoxin to the Ribosome. *Proc. Natl. Acad. Sci. U.S.A.* **2009**, *106*, 6974–6979.
- (74) Lu, B.; Cheng, X.; Huang, J.; McCammon, J. A. An Adaptive Fast Multipole Boundary Element Method for Poisson-Boltzmann Electrostatics. *J. Chem. Theory Comput.* **2009**, *5*, 1692–1699.
- (75) Gordon, J. C.; Fenley, A. T.; Onufriev, A. An Analytical Approach to Computing Biomolecular Electrostatic Potential. II. Validation and Applications. *J. Chem. Phys.* **2008**, *129*, 075102–1–075102–11.

(76) Pacios, L. F.; Garcia-Arenal, F. Comparison of Properties of particles of Cucumber mosaic virus and Tomato aspermy virus based on the analysis of molecular surfaces of capsids. *J. Gen. Virol.* **2006**, *87*, 2073–2083.

(77) Dolinsky, T. J.; Nielsen, J. E.; McCammon, J. A.; Baker, N. A. PDB2PQR: an automated pipeline for the setup, execution, and analysis of Poisson-Boltzmann electrostatics calculations. *Nucleic Acids Res.* **2004**, *32*, W665–W667.

(78) Bahadur, R. P.; Zacharias, M.; Janin, J. Dissecting Protein-RNA Recognition Sites. *Nucleic Acids Res.* **2008**, *36*, 2705–2716.